TADF versus TTA emission mechanisms in acridan and carbazole-substituted dibenzo[a,c]phenazines: Towards triplet harvesting emitters and hosts

Viktorija Andruleviciene, Karolis Leitonas, Dmytro Volyniuk, Gjergji Sini, Juozas Vidas Grazulevicius, Vytautas Getautis

Version of Record: https://www.sciencedirect.com/science/article/pii/S1385894720340213
Manuscript_082a279163620e3bc0d9dae115d8d689

TADF versus TTA emission mechanisms in acridan and carbazole-substituted dibenzo[a,c]phenazines: towards triplet harvesting emitters and hosts

Viktorija Andruleviciene[a], Karolis Leitonas[b], Dmytro Volyniuk[b], Gjergji Sini[c], Juozas Vidas Grazulevicius[b], Vytautas Getautis[a]

[a] *Department of Organic Chemistry, Kaunas University of Technology, Radvilenu pl. 19, LT-50254, Kaunas, Lithuania*

[b] *Department of Polymer Chemistry and Technology, Kaunas University of Technology, K. Barsausko g. 59, LT- 51423, Kaunas, Lithuania*

[c] *Laboratoire de Physicochimie des Polymères et des Interfaces, CY Cergy Paris Université, EA 2528, 5 mail Gay-Lussac, Cergy-Pontoise Cedex, 95031, France.*

Abstract

Carbazole or acridan-substituted dibenzo[a,c]phenazines (**CzDbp** and **AcDbp**, respectively) were synthesized and investigated exploiting the donor-acceptor-donor (D-A-D) architecture expecting thermally activated delayed fluorescence (TADF) in both cases. Unexpectedly, while experimental microseconds-lived TADF behaviour was observed for **AcDbp** efficiency of which was found to be dependent on environment, **CzDbp** exhibited nanosecond-lived fluorescence complemented by triplet-triplet annihilation (TTA). Theoretical calculations by means of the ωB97XD functional with optimally tuned range separation parameter ω, were performed for both molecules, supporting their experimentally established electrochemical, optical and photophysical properties. Using the same emitter and device structure, **CzDbp** as the bipolar host allowed to achieve by 12.5% better external quantum efficiency and better

roll-off efficiency of organic light-emitting diodes (OLEDs) in comparison to that of OLEDs based on the commercial host 1,3-bis(*N*-carbazolyl)benzene (mCP). In optimized OLED structure, device based on **CzDbp** host showed higher external quantum efficiency reaching 15.9% and lower roll-off efficiency in comparison to that of reference devices containing commercial hosts. This achievement can be explained by both the fast TTA triplet harvesting enhancing the substantial fluorescence efficiency of **CzDbp**, and by relatively high charge mobilities exceeding 10^{-3} $cm^2/V \cdot s$ for holes and 10^{-4} $cm^2/V \cdot s$ for electrons. **CzDbp** and **AcDbp** as TADF/TTA emitters were used, respectively, external quantum efficiencies of 19.4% and 22.1% for doped yellow and orange devices were achieved. The detailed discussion on TADF mechanism is presented, and the new **"dynamical" state-energy diagram** is proposed as the means allowing to better understand the TADF mechanism and the experimental results.

1. Introduction

Materials exhibiting thermally activated delayed fluorescence (TADF) have attracted significant interest in the field of organic optoelectronics.[1] TADF based organic light emitting diodes (OLEDs) can achieve 100% internal quantum efficiency (IQE), which can be attained due to harvesting of triplet excitons through the reverse intersystem crossing (RISC). Concerning TADF hosts based devices, the energy can be transmitted to the guest through the Förster energy transfer (FET) to reach 100% of its utilization. [2,3] It is well known that very small singlet–triplet energy gap (ΔE_{ST}) is essential parameter to achieve efficient TADF effect via RISC.[4] Low ΔE_{ST} can be obtained using compounds with spatially separated donor (D) and acceptor (A) units with dihedral angle between D and A fragments approaching the orthogonality.[5,6] However, the TADF efficiency is determined not only by ΔE_{ST} but also by the spin-orbit coupling (SOC). The drawback of this architecture is

consequently the smallness of SOC, which decreases in parallel with the decreasing ΔE_{ST}: due to the unification of the S_1 and T_1 character when ΔE_{ST} =0 (both become of CT nature), their coupling tends zero as stipulated by El Sayed's empirical rule.[7]

Organic materials emit prompt fluorescence even when ΔE_{ST} is too large for getting RISC However OLEDs based on prompt fluorescence with a theoretical external quantum efficiency (EQE) of 5% cannot meet the industrial requirements. TADF was observed even for compounds with relatively large ΔE_{ST}, witnessing the complexity of TADF mechanisms.[8] Organic materials with large ΔE_{ST} have big potential to be used in OLED technology when they exhibit triplet-triplet annihilation (TTA) (also co-called triplet-triplet fusion) [9, 10], "hot excitons" [11], or upper level triplet–singlet intersystem crossing [12]. In this case, two low-energy triplet excitons can be fused to one high-energy singlet exciton. In case of TTA emitters, the theoretical IQE is 62.5%, corresponding to an EQE of 12.5% of OLEDs.[9] EQE values of over 10% were reported for TTA OLEDs [13,14].

Both TADF and TTA materials can be used in OLEDs as hosts when they meet the requirements raised for host including high and balanced charge mobilities, wide transporting band gap with appropriate HOMO and LUMO energy levels for charge injection, high optical, thermal and electrochemical stability.[15,16,17] Such hosts are used not only for overcoming of aggregation induced quenching of OLED emitters in solid state and for ensuring hole-electron recombination within the light-emitting layer but also for additional triplet harvesting within host.[18] If appropriate combination of TADF host and conventional fluorescent emitter are used, OLEDs (co-called hyperfluorescent OLEDs) with 100% theoretical EQE can be fabricated. [19,20,21] While the favourable impact of TADF hosts is currently evident, knowledge on TTA OLED hosts is very limited. In this work, we partly aimed to focus on this issue. The development of efficient TADF and TTA hosts is not a

routine task since TADF and TTA materials are characterized by highly twisted molecular structures usually inducing poor charge transporting properties.

The use of theoretical predictions before synthesis of potential TADF and TTA materials is essential for saving the developing time and for getting the required properties. Time-dependent density functional theory (TDDFT) is a well-established tool to study S and T excited states of organic molecules. However, TDDFT calculations based on standard functionals can underestimate the excitation energies of the D-A molecules with the CT characteristics hence strongly impact the pertinence of theoretical diagrams of state energies. Range-separated exchange (RS) density functionals with optimally tuned range separation parameter ω were found to perform better in overcoming this problem.[22]

Here, we report on new D-A-D compounds with dibenzo[a,c]phenazine acceptor [23,24] substituted at its C-2 and/or C-7 positions by electron donating carbazole or acridan moieties [25,26]. In contrast to low-molar-mass acceptor groups such as $–CF_3$, -CN, [27], dibenzo[a,c]phenazine as the acceptor was selected expecting appropriate arrangements between planar dibenzo[a,c]phenazine units in solid films required for high electron mobility required for efficient OLED hosts [28]. The compounds were designed as TADF materials, however, contrary to the expectations, TTA was observed for the developed dibenzo[a,c]phenazine derivatives. We should note that Tang et al [29] recently reported on dibenzo[a,c]phenazine derivatives with the different number of acridan moieties at C-3 and/or C-6 positions of dibenzo[a,c]phenazine moiety. These compounds as TADF emitters demonstrated conventional TADF favourable for the fabrication of efficient orange-red OLEDs. Neither evidence of TTA nor application as hosts in OLEDs were previously reported for dibenzo[a,c]phenazine derivatives to the best of our knowledge. Since the developed here compounds demonstrated relatively high mobilities of holes and electrons, they were used not only as triplet harvesting emitters but also as triplet harvesting hosts.

Theoretical calculations were performed using ωB97XD functional with optimally tuned range separation parameter ω in order to get insight on the optical, electrochemical and photophysical properties of the compounds.

2. Experimental section

2.1. Materials

In case of OLED fabrications, commercially available molybdenum oxide (MoO_3), hexaazatriphenylenehexacabonitrile (HAT-CN), di(1-naphthyl)-N,N′-diphenyl (NPB), tris(4-carbazoyl-9-ylphenyl)amine (TCTA), 1,3-bis(*N*-carbazolyl)benzene (mCP), 3,3-di(9H-carbazol-9-yl)biphenyl (mCBP), bis(1-phenyl-isoquinoline-C2,N)(acetylacetonato)iridium(III) ($Ir(piq)_2(acac)$), 2,2',2''-(1,3,5-benzinetriyl)-tris(1-phenyl-1-H-benzimidazole) (TPBi), 2,9-Bis(naphthalen-2-yl)-4,7-diphenyl-1,10-phenanthroline (nBPhen), fluorolithium (LiF), 8-Quinolinolato lithium (Liq) were purchased from Sigma-Aldrich or Ossila and used as received.

In case of synthesis, 9,10-Phenanthrenequinone (Aldrich), *N*-bromosuccinimide (Aldrich), *o*-phenylenediamine (Aldrich), zinc chloride (Aldrich), 2-chloro-2-methylpropane (Aldrich), bis(tri-*tert*-butylphosphine)palladium(0) (Aldrich), sodium *tert*-butoxide, (Aldrich), 9*H*-carbazole (Reakhim), 9,9-dimethyl-9,10-dihydroacridine (Center for Physical Sciences and Technology) were purchased as reagent grade chemicals and used as received. 2,7-Dibromo-9,10-phenanthrenequinone, 2,7-dibromodibenzo[a,c]phenazine (**BDbp**) and 3,6-di-*tert*-butyl-9*H*-carbazole were synthesized as reported earlier.[30,31,32] Thin layer chromatography was performed by using TLC plates covered with a silica gel matrix on aluminum backing (Aldrich).

2,7-bis(3,6-di-tert-butyl-9H-carbazol-9-yl)dibenzo[a,c]phenazine (CzDbp)

BDpb (0.35 g, 0.8 mmol) and 3,6-di-tert-butyl-9*H*-carbazole (0.56 g, 2.0 mmol) was dissolved in dry toluene under argon. Then, bis(tri-*tert*-butylphosphine)palladium(0) (0.008 g, 0.016 mmol) and sodium *tert*-butoxide (0.38 g, 4.0 mmol) was added. The reaction mixture was heated at 90 °C for 24 h. After cooling to room temperature, the reaction mixture was added into water and was extracted with chloroform. The combined organic layers were washed with water and dried over anhydrous sodium sulfate. After filtration and evaporation, the crude product was purified by column column chromatography using hexane/ethylacetate (8/1) as eluent. Compound was obtained as yellow solids in 54% yield. IR (ν in cm^{-1}): 3042 (C-H ar.), 2960 (C-H alk.), 2863 (C-H alk.), 1491 (C-H alk.), 1477 (C-H alk.), 1295 (C-N), 1263 (C-N). ^{1}H NMR (400 MHz, $CDCl_3$-d_6, δ): 1.43 (s, 36H, CH_3), 7.44-7.51 (m, 8H, ar.), 7.75 (dd, *J*=6.6 Hz, *J*=3.4 Hz, 2H, ar.), 7.96 (dd, *J*=8.5 Hz, *J*=2.2 Hz, 2H, ar.), 8.15 (s, 4H, ar), 8.20 (dd, *J*=6.5 Hz, *J*=3.4 Hz, 2H, ar.), 8.72 (d, *J*=8.7 Hz, 2H, ar.), 9.61 (d, *J*=2.2 Hz, 2H, ar.). ^{13}C NMR (101 MHz, $CDCl_3$-d_6, δ): 32.1, 34.8, 109.4, 116.4, 123.7, 123.8, 124.0, 124.8, 128.6, 130.2, 130.2, 132.1, 138.1, 139.3, 142.5, 143.2. MS ($APCl^+$), *m/z* = 835 $[M]^+$. Anal calcd for $C_{60}H_{58}N_4$: C 86.29; H 7.00; N 6.71; found: C 86.29; H 6.86; N 6.98.

2,7-bis(9,9-dimethylacridin-10(9H)-yl)dibenzo[a,c]phenazine (AcDbp)

Compound was synthesized according to the same procedure as described above for the synthesis of **CzDbp**, except that 9,9-dimethyl-9,10-dihydroacridine (0.24 g, 1.1 mmol) was used instead of 3,6-di-*tert*-butyl-9*H*-carbazole. The crude product was purified by column column chromatography using hexane/ethylacetate (8/1) as eluent. It was recrystallized from eluent. Compound was obtained as orange crystals in 43% yield. IR (ν in cm^{-1}): 3059 (C-H ar.), 3033 (C-H ar.), 2954 (C-H alk.), 2924 (C-H alk.), 2853 (C-H alk.), 1475 (C-H alk.), 1449 (C-H alk.) 1325 (C-N), 1262 (C-N). ^{1}H NMR (400 MHz, $CDCl_3$-d_6, δ): 1.74 (s, 12H, CH_3), 6.35-6.37 (m, 4H, ar.), 6.88-6.93 (m, 8H, ar.), 7.46-7.48 (m, 4H, ar.), 7.76 (dd, *J*=6.3

Hz, *J*=2.9 Hz, 4H, ar.), 8.18 (dd, *J*=6.5 Hz, *J*=3.4 Hz, 2H, ar.), 8.84 (d, *J*=8.6 Hz, 2H, ar.), 9.42 (d, *J*=2.1 Hz, 2H, ar.). ^{13}C NMR (101 MHz, $CDCl_3$-d_6, δ): 31.5, 36.1, 114.2, 120.8, 125.5, 126.5, 129.5, 130.2, 140.9. MS (APCl$^+$), *m/z* = 695 $[M]^+$. Anal calcd for $C_{50}H_{38}N_4$: C 86.42; H 5.51; N 8.06; found: C 86.56; H 5.24; N 8.19

2.2. Computational methodology

The density functional theory (DFT)[33] and time dependent density functional theory (TD-DFT)[34,35,36] calculations for molecules were obtained employing the ωB97XD/6-31G(d,p) in gas phase and CPCM/ωB97XD/6-31G(d,p) in solvents where the value of the ω parameter was tuned by considering the effect of the media. Test calculations with the default ωB97XD and B3LYP functionals were also performed for the comparison of results. Up to 40 excited states were calculated by considering a band half-width at half-maximum of 0.3 eV obtaining the theoretical absorption spectra. The calculations of natural transition orbitals (NTOs) were carried out to visualize molecular orbitals of selected excited-states. The vertical ionization potentials (IP) were calculated as energy difference between neutral and cation radical species at the neutral state geometry. All calculations were performed with the Gaussian16 software.

2.3. Instrumentation

^{1}H NMR and ^{13}C NMR spectra were obtained of the solutions in deuterated chloroform ($CDCl_3$-d_6) with a Bruker Avance III spectrometer. The data are given as chemical shifts in δ (ppm) and tetramethylsilane was used as Elemental analysis was performed with an Exeter Analytical CE-440 elemental analyser, Model 440 C/H/N/. an internal standart. Mass spectra were obtained on a Waters ZQ 2000 mass spectrometer. IR spectra were recorded with a Vertex 70 Bruker spectrometer. Elemental analysis was performed with an Exeter Analytical

CE-440 elemental analyser, Model 440 C/H/N. Thermogravimetric analysis (TGA) was performed on a TA Instruments Q50 apparatus at a heating rate of 20 ºC/min under nitrogen atmosphere. Differential scanning calorimetry (DSC) measurements were performed on a 100 TA Instruments Q2000 thermal analyser at a heating/cooling rate of 10 ºC/min under nitrogen atmosphere. Optical and photophysical properties of solutions in THF, TOL and layers of the synthesized compounds were recorded using a Perkin Elmer Lambda 35 and an Edinburgh Instruments FLS980 spectrometers. Cyclic voltammetry (CV) measurements were carried out using Autolab potentiostat PGSTAT20 in a three electrode cell using platinum rod as a counter electrode, glassy carbon as working electrode and $Ag/AgNO_3$ as the reference electrode. The experiments were carried out in dry dichloromethane solution containing 0.1 M tetrabutylammonium perchlorate as electrolyte at room temperature under nitrogen atmosphere at a scan rate 50 mV/s. The measurements were calibrated using the internal standard ferrocene/ferrocenium (Fc/Fc^+). The ionization potentials (IP_{PE}) of the layers of the synthesized compounds were measured by the electron photoemission in air method.[37] Hole drift mobility of the materials was estimated by a time-of-flight (TOF) method. The samples were fabricated with structures of ITO/compound/Al. Commercial indium tin oxide (ITO) coated glass was used as a substrate, which was first cleaned chemically using a bath of distilled water and acetone. Organic and Al films were sequentially vacuum-deposited onto precleaned ITO-coated glass substrates under the vacuum of $2\text{-}5 \cdot 10^{-6}$ mBar using vacuum equipment from Kurt J. Lesker in-built in an MB EcoVap4G glove box. In the TOF experiments, charges were generated by a pulsed third-harmonic Nd:YAG laser EKSPLA NL300 working at a pulse duration of 3-6 ns and the wavelength of 355 nm. Electric fields were applied by a Keithley 6517B electrometer. A digital storage oscilloscope Tektronix TDS 3032C was used to record TOF transients. The drift mobility was calculated by using the formula $\mu = d^2/U \cdot t_t$, where d is the layer thickness, and U the surface potential at the

moment of illumination, and t_t is the transit time which was taken from the TOF transients. A Keithley source meter 2400-C was utilized for recoding of the current density-voltage characteristics. The current density–luminance characteristics were estimated using a calibrated silicon photodiode with the 6517B Keithley electrometer. Electroluminescence (EL) spectra were recorded by an Avantes AvaSpec-2048XL spectrometer. The current, power and external quantum efficiencies were estimated utilizing the current density, luminance, and EL spectra as reported earlier.[38]

3. Results and discussion

3.1. Synthesis

As shown in **Scheme 1**, we designed and synthesized compounds with donor–acceptor–donor (D–A–D) architecture composed of dibenzo[a,c]phenazine (**Dbp**) acceptor core and peripheral aromatic donor moieties such as 9,9-dimethylacridine (**Ac**) and 3,6-di-tert-butyl-carbazole (**Cz**). The intermediate compound **BDbp** was prepared through a condensation reaction between 2,7-dibromo-9,10-phenanthrenequinone and *o*-phenylenediamine. The Buchwald–Hartwig amination of **BDbp** with 3,6-di-tert-butyl-9*H*-carbazole or 9,9-dimethyl-9,10-dihydroacridine in the presence of bis(tri-tert-butylphosphine)palladium(0) as a catalyst afforded **CzDbp** and **AcDbp**, respectively. The target products were purified by column chromatography. Their chemical structures were confirmed by ^{1}H and ^{13}C nuclear magnetic resonance (NMR), IR spectroscopies, mass spectrometry and elemental analysis.

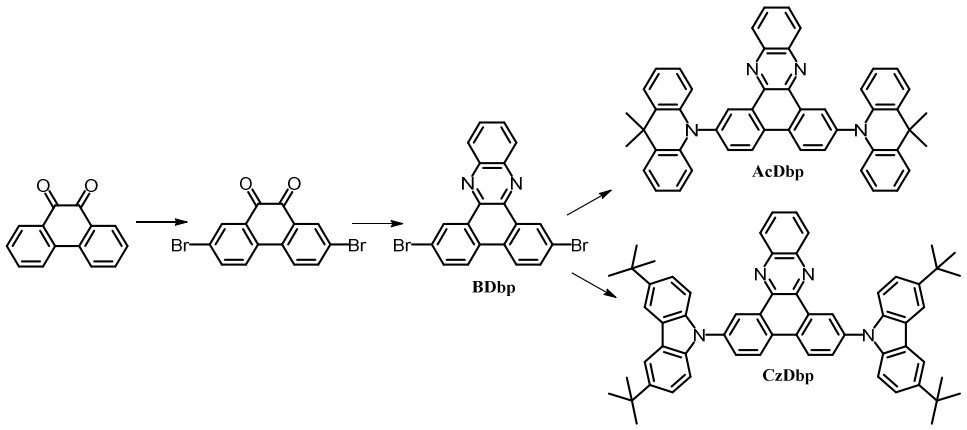

Scheme 1. Synthetic route for **AcDbp** and **CzDbp.**

3.2. Computational details

Theoretical calculations were performed using ωB97XD functional with optimally tuned range separation parameter in toluene (TOL) and tetrahydrofuran (THF). Solvents effect was taken into account within the conductor-like polarizable continuum model (CPCM). The ω values were optimally tuned by minimizing a function J(ω), where ε_{HOMO} and ε_{LUMO} denote the energies of the HOMO and LUMO, IP and EA are the vertical ionization potential and electron affinity of the molecule, respectively:[39]

$$J(\omega) = [\varepsilon_{HOMO}(\omega) + IP(\omega)]^2 + [\varepsilon_{LUMO}(\omega) + EA(\omega)]^2$$

Calculations using ωB97XD ($\omega^{default}$), ωB97XD with ω tuned in gas (ω^{gas}) and B3LYP functionals were performed for the comparison of the obtained results, and the corresponding results are shown in the **Annex I** (Supporting information).

3.3. Geometry and Molecular orbitals

Theoretical calculations performed with ω tuned in solvents revealed that dihedral angles between **Dbp** and **Ac** fragments is 90° in **AcDbp** (**Table 1**). While analogous dihedral angle between **Dbp** and **Cz** moieties in **CzDbp** is affected by the ω meaning of ωB97XD functional. **Table 1** indicates that the dihedral angle D-A obtained with the lower ω=0.0011

Å^{-1} is ~76° and that calculated with the higher ω=0.0337 Å^{-1} is ~61°. The larger dihedral angles in the case of **AcDbp** are due to the shorter (C-)H….**Dbp** distances as compared to **CzDbp**, in turn stemming from the larger C-C-C angle in the six-atom central ring in **Ac** as compared to five-atom central ring in **Cz** (~122° and ~108° respectively). The HOMO of **AcDbp** is distributed on the both peripheral **Ac** units, whereas the LUMO is localized exceptionally over the molecule **Dbp** core (**Fig. 1**). The spatial separation of the HOMO and LUMO appears because of the perpendicular dihedral angles D-A. In the case of **CzDbp**, HOMO of **CzDbp** at ω^{TOL} B97XD is localized on the **Cz** moieties extending to the **Dbp** core, while calculations at ω^{THF} B97XD show HOMO localization on the donor fragments, with less contribution from the **Dbp** (**Fig. 1**). As for LUMO of **CzDbp**, in both cases it is localized on the acceptor core.

Table 1. Inter-fragment dihedral angles (degrees), energies of frontier orbitals and vertical ionization potential values for compounds **AcDbp** and **CzDbp** calculated at the DFT/6-31G**

	ωB97XD			
	ω^{THF}=0.0011Å^{-1}	**ω^{TOL}=0.0337 Å^{-1}**	**ω^{THF}=0.0011Å^{-1}**	**ω^{TOL}=0.0322 Å^{-1}**
	AcDbp		**CzDbp**	
dihedral angle	90.1	90.3	75.6	60.7
HOMO, eV	-5.01	-5.34	-5.31	-5.56
LUMO, eV	-2.30	-1.91	-2.31	-1.91
IP^{teor}, eV	4.98	5.28	5.28	5.49

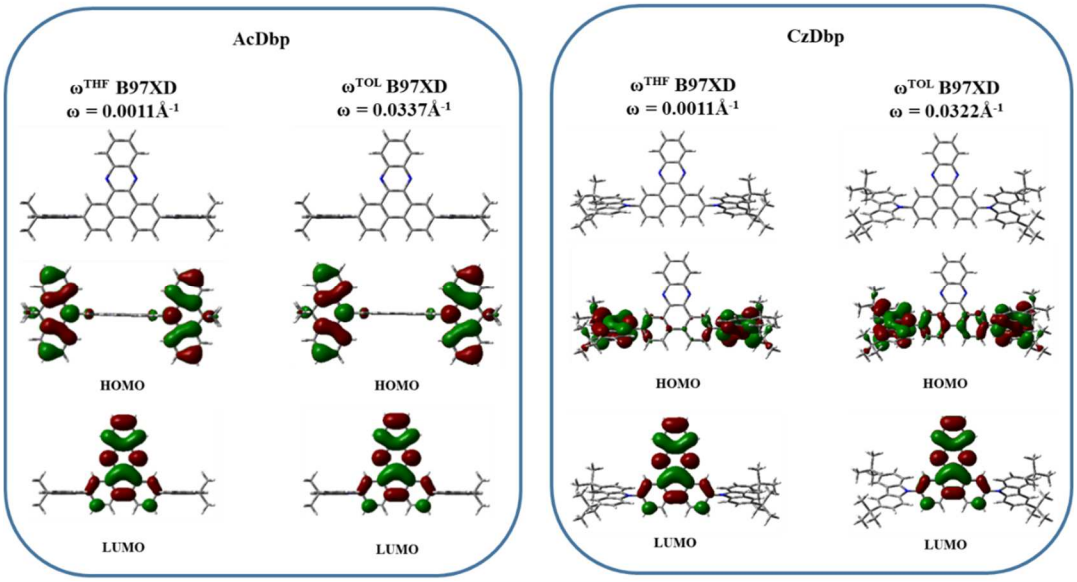

Fig. 1. Geometry and plots of frontier orbitals of **AcDbp** and **CzDbp** at B97XD calculated with ω tuned in THF and TOL.

3.4. Ionization potentials and charge mobilities

The ionization potentials (*IP*) of investigated materials were estimated using photoelectron emission (PE) method in air (**Fig. S1**) and cyclic voltammetry (CV) (**Fig. S2**). The same IP^{PE} value of 5.5 eV for **AcDbp** and **CzDbp** was found which is larger as compared to the IP^{CV} values of 5.25 eV and 5.44 eV, respectively (**Table 2**). The difference stems from the stronger polarization effects in the solid state (PE measurements). Additionally, CV measurements reveal reduction peaks of the compounds which were used to estimate electron affinity (EA^{CV}) values of 3.12 eV for **AcDbp** and 3.11 eV for **CzDbp** (**Table 2**). The values of EA^{PE} were obtained from the IP^{PE} values and the optical band gaps (E_g,^{opt}), which were deduced from the edges of the absorption spectra of the vacuum deposited layers (**Fig. S3**). The calculated EA^{PE} value of **AcDbp** was by 0.24 eV higher than that of **CzDbp** (2.77 eV and 2.53 eV, respectively). The difference between CV and PE values stem from not only the

environmental polarization effects, but also from the fact that the optical gap values used in the calculation of EA^{PE} are larger than the IP^{CV}-EA^{CV} gap by 0.6 eV and 0.64 eV of **AcDbp** and **CzDbp**, respectively, corresponding to the electron-hole binding energy in the first excited state. In order to extend theoretical investigation of the compounds, IP^{theor} values were calculated. The analysis revealed, that experimental IP^{CV} values of 5.25 eV and 5.44 eV well coincide with the values of IP^{theor} obtained by ω^{TOL} B97XD of 5.28 eV and 5.49, respectively (**Table 1,2**).

Table 2. Ionization potential, electron affinity and charge mobility data for **AcDbp** and **CzDbp**

	IP^{PE}, eV	E_g,^{opt} eV	EA^{PE}, eV	IP^{CV}, eV	EA^{CV}, eV	μ_h^*, cm^2/Vs	μ_e^*, cm^2/Vs
AcDbp	5.50	2.73	2.77	5.25	3.12	$2.4 \cdot 10^{-3}$	$1.2 \cdot 10^{-3}$
CzDbp	5.50	2.97	2.53	5.44	3.11	$3.8 \cdot 10^{-3}$	$1.0 \cdot 10^{-4}$

* charge mobility at $2.02 \cdot 10^5$ V/cm

Charge transporting properties of the vacuum deposited layers of **AcDbp** and **CzDbp** were characterized by time-of-flight (ToF) technique. ToF current transients with well recognized transit times were recorded applying positive and negative electric fields (**Fig. S4**). These results show that solid layers of **AcDbp** and **CzDbp** are able to transport both holes and electrons (**Fig. 2a**). The layers of compounds showed charge-drift mobilities exceeding 10^{-3} cm^2/Vs at high electric fields except the electron-drift mobility in the layer of **CzDbp** which was by one order of magnitude lower. The lower electron mobility of **CzDbp** may stem from the smaller D-A dihedral angle which might result in larger disorder in packing between LUMO-containing moieties. Compound **CzDbp** exhibits flexible D-A dihedral angle of ca. 76° in THF and of ca. 61° in toluene, which allows for non-negligible pi-orbital overlaps between donor and acceptor. Meanwhile, **AcDbp** exhibits constrained angle (of ca. 90° in

THF and toluene) because of the rigidity of acridan moiety which is translated in practically zero overlaps between donor and acceptor moieties. On the other hand, the impact of dihedral oscillations is minimal around zero (dihedrals of 90°) as compared to smaller dihedral angles (faster evolution of overlaps). As a result, the D-A dihedral angle in the solid-layer of **CzDbp** can change in a wider range causing variations in molecular geometry, an increase of the geometrical randomness component of the energetic disorder [40], resulting in reduced electron-drift mobility.

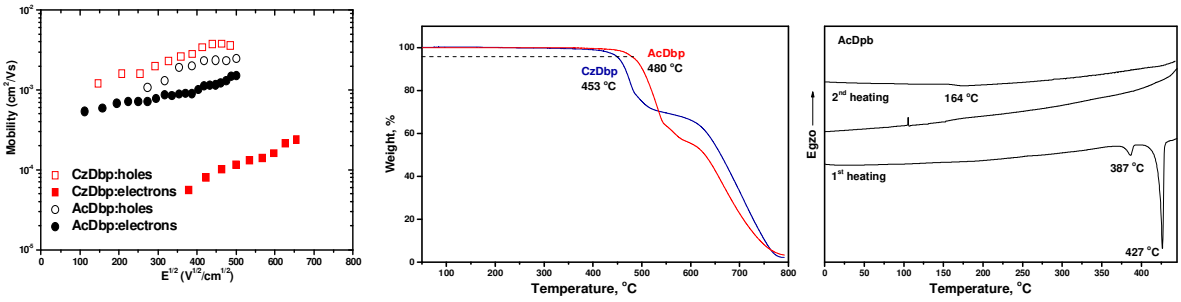

(a) **(b)** **(c)**

Fig. 2. Electric field dependences of charge mobilities for the layers **(a)** of **AcDbp** and **CzDbp,** TGA curves of **AcDbp** and **CzDbp (b)** and DSC curves of **AcDbp (c).**

In addition, the smaller electron mobility of **CzDbp** may result from the *tert*-butyl substituents of carbazole moieties**.** *Tert*-butyl substituents apparently increase the distance between neighboring **CzDbp** molecules in the solid films. The increased intermolecular distance may also reduce LUMO-LUMO overlapping between neighboring molecules causing difficulties for electron hoping, thus causing the lower electron mobility of **CzDbp** relative to that of **AcDbp** containing the same electron-accepting unit dibenzo[a,c]phenazine but unsubstituted donor moieties.

3.5. Thermal characteristics

AcDbp and **CzDbp** showed high thermal stability with 5% weight loss at 480 °C and 453 °C, respectively, as confirmed by thermogravimetric analysis (TGA) (**Fig. 2b**). The morphological transitions of the compounds were investigated by differential scanning calorimetry (DSC). **Fig. 2c** shows DSC heating and cooling curves for **AcDbp.** This compound was obtained after the synthesis and purification as the crystalline substance. It showed two endothermic melting signals at 387 °C and 427 °C during the first DSC heating scan. The cooling and the second heating scans revealed only a glass transition at 164 °C. In the heating and cooling scans of **CzDbp** no signals of melting, crystallization or glass transition were observed (**Fig. S5**).

3.6. Photophysical properties

Absorption. The experimental absorbance spectra of **AcDbp** and **CzDbp** were compared with the computed ones at the TD-DFT level with $\omega^{THF,TOL}$ B97XD (**Fig. 3**). The position of theoretical absorption bands of **AcDbp** and **CzDbp** were in good agreement with the experimental ones. This observation can be related to the improved description of origin of excitations provided by the optimization of the ω. Analysis of the most intense transitions (**Table S1**) revealed that absorption band at 370 nm of **AcDbp** described transition $S_0 \rightarrow S_9$. In order to identify the nature of transition, natural transition orbitals (NTO) were calculated which showed that this absorption band of **AcDbp** is associated with the local electronic excitations in **Dbp** core (**Fig. S6**). Meanwhile, absorption band at 350 nm of **CzDbp** obtained at ω^{THF} B97XD and ω^{TOL} B97XD corresponds to the combination of electronic transitions towards two excited states of S_8, S_9 and S_7, S_9, respectively (**Table S1**). According to the NTO, $S_0 \rightarrow S_8$ and $S_0 \rightarrow S_7$ are dominated by the charge transfer from **Cz** units to **Dbp** core, with small contribution from the local **Dbp** excitations, and $S_0 \rightarrow S_9$ is associated only with the local electronic transitions in **Dbp** core (**Fig. S6**).

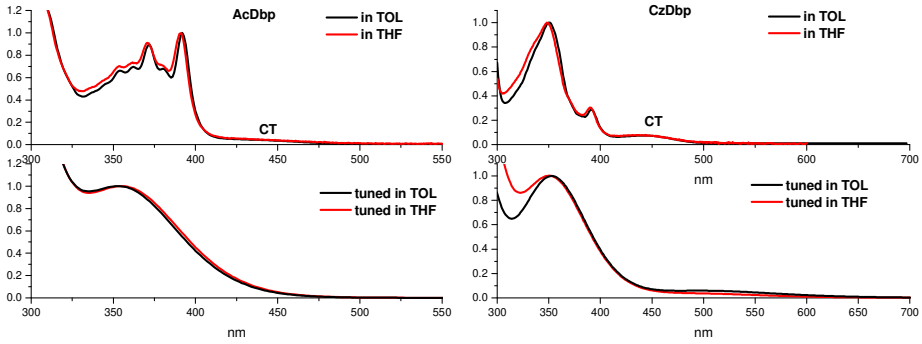

Fig. 3. Experimental and theoretical absorption spectra of **AcDbp** and **CzDbp**

The theoretical results indicate that the six lowest energy transitions (S_1-S_6) of **AcDbp** demonstrate charge transfer (CT) from donors to acceptor, exhibiting practically zero oscillator strengths due to the orthogonal geometry of the molecule (**Table S1**). However, experimental spectra of the solutions in tetrahydrofuran (THF) and toluene (TOL) exhibit a weak CT tail in the region of 400-500 nm (**Fig. 3**). This suggests an increased oscillator strength for the CT states stemming due to shifted dihedral angle from 90° between **Ac** and **Dbp**. While the lowest energy transitions S_1-S_4 for **CzDbp** correspond to the CT between donors and acceptor giving a small intensity band in the range 450-600 nm (**Table S1**).

The larger absorption intensity of CT bands in experimental absorption spectra as compared to theoretical ones can be observed. This observation can be explained by the smaller dihedral angle D-A of molecules than the theoretical calculated ones (**Fig. 3**). The intramolecular differences may appear due to some degree of aggregation in the ground state in solutions. To check such assumption, the absorption spectra of the different concentrations of AcDbp and CzDbp in TOL and THF solutions revealed increase of intensity of CT bands when concentrations of the compounds in solutions increases (**Fig. S7**). Such differences revealed presence of aggregates in the solutions. The theoretical calculations confirmed that oscillator strength of the CT states depends on the size of dihedral angle D-A. The smaller

dihedral angle resulted in the larger value of oscillator strengths at S1 state for AcDbp and CzDbp (**Table S2**).

Emission. Fluorescence spectra and photoluminescence quantum yield (PLQY) of the solutions of **AcDbp** and **CzDbp** in the solvents of different polarity (ε^{TOL}=2.38 and ε^{THF}=7.50) were recorded (**Table 3, Fig. 4a**). Both the compounds exhibited structureless PL profiles, indicating CT nature of the emissive states. This observation is in line with the nature of the lowest absorption bands in solutions of **AcDbp** and **CzDbp**. The stronger solvatochromic effect was detected in the fluorescence spectra of the solutions of **AcDbp** compared to those of **CzDbp** because of the dominant CT nature in **AcDbp**, which is coherent with the corresponding D-A dihedral angle, hence the purer CT states in the case of **AcDbp** as compared to **CzDbp**. Solutions of **CzDbp** showed higher values of PLQY than solutions of **AcDbp** (**Table 3**). The values of PLQY of the solutions in TOL and THF of **AcDbp** were 2% and 0.5% while those of the solutions of **CzDbp** were 37% and 28%, respectively. Again, these results are in line with the corresponding geometries, the orthogonal D-A geometry in **AcDbp** preventing from any efficient $S_1 \rightarrow S_0$ fluorescence in spite of the efficiency of the triplet→singlet conversion efficiency. Indeed, the theoretical results indicate a dark S_1 state in the case of **AcDbp** (zero oscillator strength), as compared to 0.023 for **CzDbp** (**Table S1**).

The measurements of the degassed solutions showed interesting differences: while solutions of **AcDbp** showed insignificant increase of PLQY, **CzDbp** demonstrated increase of PLQY by 16% for both the solutions, which, as we show below, could stem from TTA. To support this assumption, the plots of PL intensity versus excitation intensity ($\lambda_{excitation}$=400 nm) (**Fig. S8**) were recorded for powders and THF solutions (0.5 mg/ml) of **AcDbp** and **CzDbp** using neutral filters according to the method described in ref. [41]. Integrated PL intensities versus

excitation intensities for powders and THF solutions of **AcDbp** and **CzDbp** are plotted in **Fig. 4b**. The linear fits of these dependences in the different excitation intensity ranges (9-100% (**Fig. 4b**) and 24-100 %(**Fig. 4b** inset)), revealed the slopes higher than unity displaying contribution of TTA emission [9,10,13,14,41].

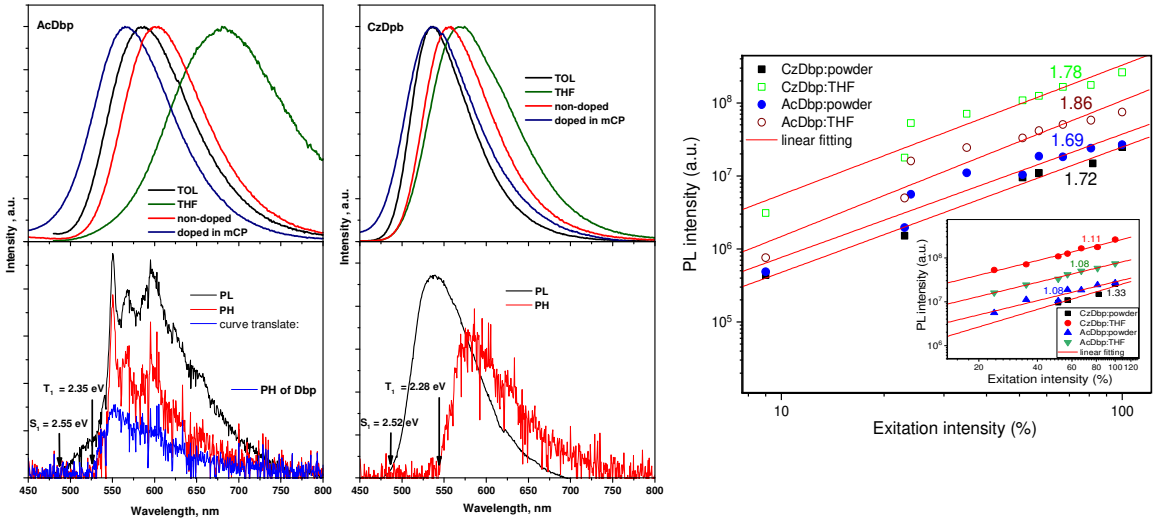

(a) **(b)**

Fig. 4. Room-temperature fluorescence spectra and photoluminescence as well as phosphorescence spectra recorded at 77 K of THF solutions of **AcDbp** and **CzDbp** (phosphorescence spectrum of the solution of **Dbp** in THF recorded at 77 K is presented as blue line) **(a)** and plots of integrated PL intensities versus excitation intensities for powders and THF solutions of **AcDbp** and **CzDbp (b).**

The onsets of photoluminescence (PL) and phosphorescence (PH) spectra of the solutions of **AcDbp** and **CzDbp** in THF recorded at 77 K were used to estimate singlet-triplet energy differences (ΔE_{ST}) (**Fig. 4a, Table 3**). The PL spectrum of **AcDbp** exhibited a structureless shoulder with the onset estimated at 2.55 eV (**Fig. 4a**), indicative of CT nature of the emissive state. This observation is in line with the lowest energy band of the corresponding absorption spectra. PH spectrum of **AcDbp** showed characteristic vibrational structure, indicating that the lowest emissive T_1 state at 77 K corresponds to the local excitation (^{3}LE)

of **Dbp**-core. As for, Both PL and PH spectra of THF solution of **CzDbp** exhibited broad and structureless emission indicating CT nature of S_1 and T_1 excited states. Analysis of molecular orbitals of **AcDbp** and **CzDbp** indicates that for both the compounds, ^{1}CT and ^{3}CT occur due to transition from donor to acceptor, while ^{3}LE transition takes place between orbitals delocalized over the **Dbp** core (**Fig. S9, S10**).

Table 3. Photophysical properties of **AcDbp** and **CzDbp**

	$PLQY^{under\ air}$,%*	$PLQY^{degassed}$, %	S_1,eV	T_1,eV	ΔE_{ST},eV
	THF/TOL/non-doped/mCP/mCBP	THF/TOL	THF		
AcDbp	0.5/2/3/4/8	0.6/3	2.55	2.35	0.20
CzDbp	28/37/15/11/21	44/53	2.52	2.28	0.24

* measured at air condition.

The experimental estimation of the singlet-triplet energy splitting (ΔE_{ST}) revealed values of 0.24 eV and 0.20 eV for **CzDbp** and **AcDbp**, respectively. The experimental ΔE_{ST} value for **CzDbp** is in good agreement with the theoretical vertical ΔE_{ST} values of 0.20 eV (THF) and 0.21 (TOL) (**Table S2, and Fig. S11**). However, for acridan-containing compound (**AcDbp**) the theoretical vertical ΔE_{ST} value is zero (**Table S2, Fig. S11**). The dichotomy between theory and experiment is also witnessed by the different nature of the corresponding lowest triplet state. While the experimental emissive triplet state is a local one of 2.35 eV (PH spectrum in **Fig. 4a**), the theoretical LE corresponds to T_3 at 2.33 eV, T_1 and T_2 being of CT nature (**Fig. S10, S11**). Interestingly, the lowest energy absorption band in the experimental absorption spectrum of **AcDbp** is a CT one (**Fig. 3**). A recent report [42] indicated that THF becomes solid at 77K and geometric relaxation of the solvent is no longer possible. This effect was shown to blue-shift the PL maximum at 77 K by roughly 0.4 eV as compared to room temperature, which was traced back to the inefficient stabilization of the emissive CT state. Following these results, it is possible that CT in **AcDbp** is not entirely stabilized by

solvent, thus resulting in emission from LE state. In the case of **CzDbp,** CT state could be stabilized by the electronic polarization of the adjacent **CzDbp** molecules [42], given that this compound was found to form aggregates (**Fig. S7**).

PL spectra and PL decay curves of the solutions of **AcDbp** and **CzDbp** in TOL and THF were recorded before and after degassing. As shown in **Fig. 5** and **Fig. S12**, the solution of **AcDbp** exhibited double exponential decay. The air equilibrated TOL and THF solutions showed lifetimes of long-lived component (τ_2) of 362 ns and 420 ns, respectively. Meanwhile, under oxygen free conditions τ_2 increased to 10946 ns for TOL solution and 2437 ns for THF solution suggesting a radiative PL stemming from triplet harvesting assumedly through TADF. The shapes of emission spectra of non-degassed and degassed solutions of the compounds were very similar showing that delayed fluorescence originated from the same CT state as prompt fluorescence (**Fig. 5,S11**). Intriguingly, the solutions of **CzDbp** in TOL and THF exhibited single exponential PL decays showing only prompt fluorescence (**Fig. 5,S11**). The solutions of **CzDbp** exhibited increase of PLQY by 16% after deoxygenation. This observation shows that the triplet states do play a role in the PL of **CzDbp**, which should consequently be realized through a channel different from TADF, being as fast as the prompt fluorescence.

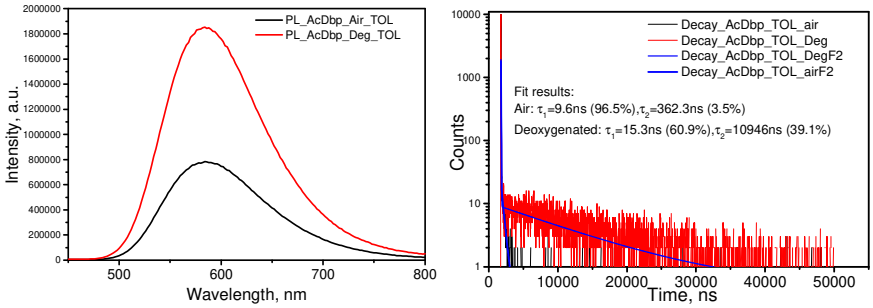

(a) **(b)**

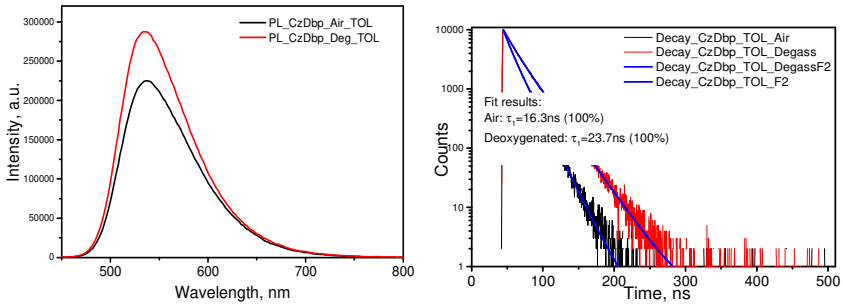

(c) **(d)**

Fig. 5. PL spectra (left) and PL decay curves (right) of air equilibrated and deoxygenated solutions of **AcDbp** (**a-b**) and **CzDbp** (**c-d**) in TOL

Since the delayed fluorescence can be activated by temperature, PL spectra and PL decay curves of non-doped and doped (10 wt. %) in mCP layers of **AcDbp** and **CzDbp** were recorded at the different temperatures ranging from 77K to 300 K (**Fig. 6, S13, S14**). The PL intensities, thus absolute PLQYs of the layers of both non-doped AcDbp and doped in mCP increased when the temperature was increased from ca. 220 K to 300 K (**Fig. S14**) Such increase of PL intensity with increasing temperature can be explained by TADF contribution [1]. However, the intensity of the decay profile of delayed fluorescence, thus contribution of delayed fluorescence (τ_{TADF}), decreases with an increase of temperature for the layer of non-doped **AcDbp** (**Fig. 6b**). Such PL decay behaviour under different temperatures for TADF compounds are not typical and it is rarely described/discussed in the literature [41,43]. For example, J. Grüne at. el. demonstrated that negative temperature dependence of the transient electroluminescent decays at increasing temperature of exciplex-based TADF emitters are mainly related to contribution of TTA [41]. We found similarities between PL decay behavior under different temperatures of the layer of **AcDbp** and temperature-dependent transient electroluminescence (EL) decays of OLED with emission layer of m-MTDATA:3TPYMB described in ref. 41. Precise fitting of the temperature-dependent transient EL decays in ref. 41 proved that unusual temperature-dependent transient EL decays are mainly related to TTA. Since experimental evidence of TTA was also obtained for compounds

AcDbp(CzDbp), the obtained unusual temperature-dependent PL decays of **AcDbp(CzDbp)** are also related to TTA emission mechanism.

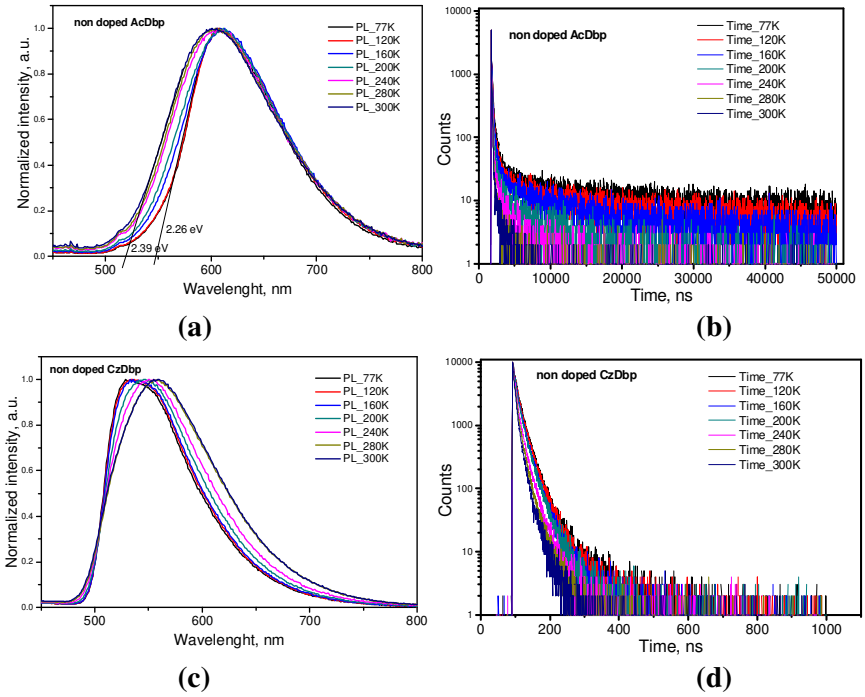

Fig. 6. PL spectra (left) and PL decay curves (right) of the layers of non-doped **AcDbp** (**a**-**b**) or **CzDbp** (**c**-**d**) recorded at different temperatures

To demonstrate more evidences of TADF for **AcDbp**, from the plots of RISC rate versus temperature at the temperatures exceeding 200K (at which phosphorescence is absent) by Arrhenius equation [44] (**Fig. S15**), activation energies (E_a) of 72 and 55 meV were obtained for the layers of non-doped and doped in mCP of 10 wt.% **AcDbp**. Relatively low E_a values and small difference between the values of the layers of non-doped and doped **AcDbp**. Such result is in agreement with low ΔE_{ST} value for **AcDbp** (**Table 3**). Thus, population of the emissive singlet state via RISC from the triplet state is allowed. Such E_a values are in good agreement with corresponding values of previously reported TADF compounds. [45,46]

PL decay curves of the layers of **CzDbp**, in the temperatures ranging from 77 K to 300 K revealed only prompt fluorescence. No long-lived components assigned to

phosphorescence or delayed fluorescence were detected (**Fig. 6d, S13d**). No phosphorescence was experimentally observed neither for the layer of non-doped **CzDbp** nor for that of doped 10 wt.% **CzDbp** in mCP. It should be noted that the intensity of the PL decay profile decreases with increasing of temperature for the non-doped **CzDbp** because of the TTA as it was mentioned above (**Fig. 6d**). For **CzDbp**, no delayed fluorescence was recorded. The reasons are additionally discussed in the section "**Mechanistic considerations**".

3.7. Electroluminescent properties

Compound **AcDbp** has potential as TADF host for red OLEDs taking into account its charge-transporting properties, energy of first triplet level, and ability to exhibit TADF. On the other hand, **CzDbp** showed ambipolar charge-transporting properties and higher PLQY than **AcDbp**. Consequently, both **AcDbp** and **CzDbp** were use in PHOLED, in order to demonstrate their suitability as host materials for a commercial red phosphorescent emitter $(piq)_2Ir(acac)$. The analogous PHOLED based on well-known host **mCP** was also fabricated for comparison. All functional layers in the fabricated PHOLEDs were the same except light-emitting layers. Three devices with the configuration ITO/ MoO_3 (0.6nm)/NPB (30 nm)/5 wt.% (piq)2Ir(acac): **AcDbp** or **CzDbp** or **mCP** (20 nm)/TPBi (70 nm)/LiF (0.8nm):Al fabricated using hosts **AcDbp, CzDbp** or **mCP** were named as devices **A, B**, or **C**, respectively (**Fig. 7, Table 4**).

PHOLEDs **A**, **B** and **C** showed classical $(piq)_2Ir(acac)$ emissions with the peak wavelength of 623 nm (**Fig. S16**). Only the emission of phosphorescent emitter was observed in electroluminescence spectra of devices **A** and **B**, manifesting complete energy transfer from host to $(piq)_2Ir(acac)$. In the case of PHOLED C, additional weak emission in the range 350-500 nm is detected since the mCP host is not the best host for the selected red phosphorescent

$(piq)_2Ir(acac)$. As it will be discussed below, no additional bands were observed when a more appropriate host was selected for the reference device (**Fig. 8a,S20-24**).

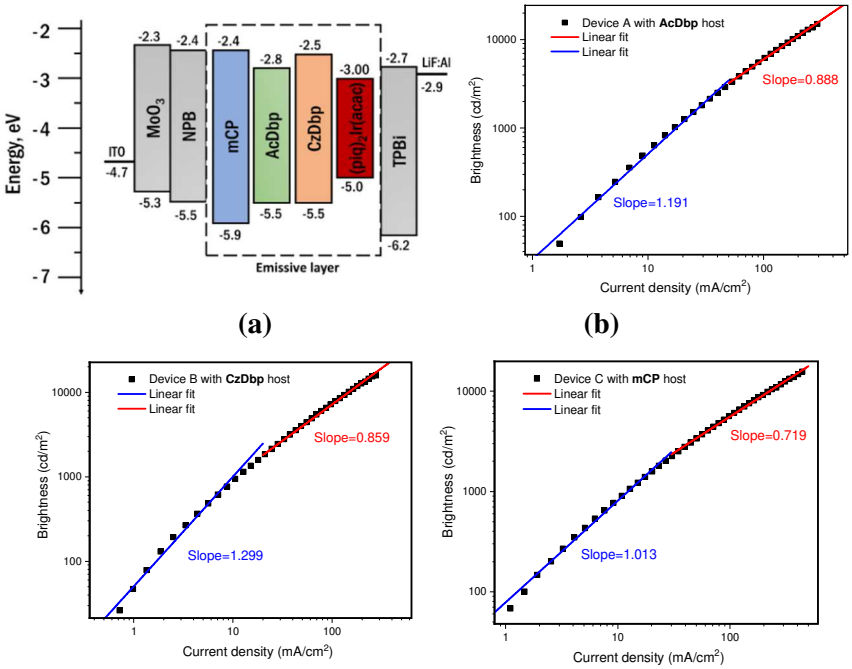

Fig. 7. Equilibrium energy diagram (a) of devices **A**-**C**. IP^{PE} and EA^{PE} values of solid smples of **AcDbp** and **CzDbp** were taken for the design of the device structures (**Table 2**). Linear fits to current density versus brightness plots for devices **A**-**C** (b-d).

Devices **A** and **B** exhibited lower turn-on voltage (V_{on}) compared to that of device **C** indicating excellent electron and hole injection (**Fig. S17**). The best maximum current efficiency (CE_{max}), maximum power efficiency (PE_{max}) and external quantum efficiency (EQE_{max}) was demonstrated by device **B** with **CzDbp** as a host (**Fig. S18**). Higher EQE_{max} of 9% was obtained for **CzDbp**-based PHOLED **B** in comparison to EQE_{max} of 8% observed for the reference mCP-based device **C**. Knowing that mCP is one of the best conventional host, the result is exciting and is apparently related to the additional triplet harvesting by host via TADF or TTA. To further study EL characteristics of devices **A**-**C**, brightness versus current

density were plotted in log-log scales. Two different linear regions can be recognized and linearly fitted ($1>R^2>0.98$) (**Fig. 7 b-d**, **S19**). At low current density, the slope of ca. 1 (1.013) was obtained for mCP-based device **C**, which is typically expected for conventional fluorescent and phosphorescent OLEDs where one photon is created by recombination of one exciton.[47] However, despite the same emitter used, the slopes higher than unity were obtained for devices **A** and **B** at low current density (**Fig. 7b,c**). This result points to some contribution from the TTA mechanism, given that harvesting of 100% of triplets by means of the TTA manifests with the slope reaching the value of 2.[13,48,49] This observation indicates that electroluminescence of devices **A** and **B** is related to both emission of the $(piq)_2Ir(acac)$ and emission enhancement by TTA mechanism. It should be noted, that TTA efficiency of host **CzDbp** should be higher than that of host **AcDbp**. The corresponding slope (1.299) of device **B** is higher than that (1.191) of device **A**.

At high current density, the slopes of all devices **A**-**C** were lower than unity which is related to the efficiency roll-off (**Fig. 7b-d, S19**). Efficiency roll-off of devices **A** and **B** was lower (the slopes are closer to the unity) than that of device **C**. This observation additionally highlights higher efficiency of the developed TADF/TTA hosts in comparison to the conventional mCP.

Table 4. EL parameters of the devices **A**-**J**

Device	Emissive layer	[a]V_{ON}/	CE_{max},	PE_{max},	EQE_{max},	CIE 1931

		[b]$V_{Driving}$, V	cd/A	lm/W	%	(x, y)
Host tests using structure: ITO/MoO_3/NPB/ Emissive layer /TPBi/LiF:Al						
A	$(piq)_2Ir(acac)$:**AcDbp**	3.0/3.85	6.3	4.6	6.0	(0.658, 0.340)
B	$(piq)_2Ir(acac)$:**CzDbp**	3.4/4.5	9.0	6.4	9.0	(0.655, 0.343)
C	$(piq)_2Ir(acac)$:**mCP**	4.0/5.2	8.6	5.6	8.0	(0.633, 0.329)
Host tests using structure: ITO/HAT-CN/NPB/TCTA/mCBP/ Emissive layer /nBPhen/Liq/Al						
D	$(piq)_2Ir(acac)$:**AcDbp**	3.2/5.2	9.8	9.1	13.2	(0.671, 0.324)
E	$(piq)_2Ir(acac)$:**CzDbp**	3.0/4.75	10.3	11.6	15.9	(0.677, 0.32)
F	$(piq)_2Ir(acac)$:**mCBP**	2.9/4.0	11.5	12.9	13.1	(0.674, 0.322)
G	$(piq)_2Ir(acac)$:**NPB**	3.2/4.5	6.6	6.7	9.0	(0.665, 0.32)
H	$(piq)_2Ir(acac)$:**nBPhen**	4.8/8.7	12.5	8.5	14.6	(0.677, 0.318)
Emitter tests using structure: ITO/HAT-CN/NPB/TCTA/mCBP/ Emissive layer /nBPhen/Liq/Al						
I	**AcDbp**:mCBP	3.6/6.7	41.6	35.3	19.4	(0.513, 0.479)
J	**CzDbp**:mCBP	3.7/7.0	54.4	46.2	22.1	(0.395, 0.578)

[a]V_{ON} was taken at 10 cd/m^2; [b]$V_{Driving}$ was taken at 10 mA/cm^2; [c]CIE (x,y) was taken 1000 cd/m^2

With the aim of additional optimization of device structure, five devices with the configuration ITO/HAT-CN(5 nm)/NPB(40 nm)/TCTA(10 nm)/mCBP(10 nm)/ 5wt. % $(piq)_2Ir(acac)$: **AcDbp** or **CzDbp** or **mCBP** or **NPB** or **nBPhen** (50 nm)/nBPhen (30 nm)/Liq(2 nm)/Al were fabricated using hosts **AcDbp, CzDbp, mCBP**, **NPB,** or **nBPhen** and named as devices **D, E**, **F, G** or **H**, respectively (**Fig. 8, Table 4**). EL spectra recorded at the different voltages of PHOLEDs **D**-H were completely related to $(piq)_2Ir(acac)$ emissions (**Fig. 8a, S20-S24**). Due to improved charge-injecting properties, $(piq)_2Ir(acac)$-based devices **D-H** exhibited improved out-put electroluminescent characteristics. Device **E** fabricated using the developed host **CzDbp,** demonstrated the higher maximum EQE (15.9 %) in comparison to the reference devices **F-H** containing **mCBP**, **NPB** or **nBPhen** as hosts (**Fig. 8b, S20-S24, Table 4**). The differences between EQE values of device **E** and **F-H** are related

to either their different charge-balance factors (γ), efficiency of exciton production (χ), PLQY or the outcoupling efficiency (η_{out}) according to the formula [48]

$$EQE=\gamma\times PLQY\times\chi\times\eta_{out} \quad (1).$$

Since the thicknesses of all functional layers and device structure of OLEDs **D-H** was the same, their outcoupling efficiency should be similar. It should be noted that the layers 5wt. % solid solutions of $(piq)_2Ir(acac)$ in **mCP, NPB** or **nBPhen** (9, 15, or 7 %, respectively) showed slightly higher PLQY values than 5wt. % solid solutions of $(piq)_2Ir(acac)$ in **AcDbp** and **CzDbp** (7 and 8%, respectively) (**Fig. S25**). The different PLQYs of $(piq)_2Ir(acac)$ can be related to higher polarity of donor-acceptor-donor type hosts **AcDbp** and **CzDbp** hosts than that of electron donating hosts **mCP**, **NPB** and electron-accepting host **nBPhen**. Thus, the higher maximum EQE of device **E** is not related to the higher PLQY of the light-emitting layer of 5wt. % solid solution of (piq)2Ir(acac) in **CzDbp**. It should be noted that the values of PLQYs recorded for $(piq)_2Ir(acac)$ dispersed in the different hosts are lower than the previously reported PLQY (20%) of the same emitter [50]. Such differences were apparently obtained since the above PLQYs were taken under air conditions. In any case, the obtained PLQYs should not be used for the calculation of the theoretical maximum EQE for $(piq)_2Ir(acac)$-based devices by formula (1). It is known that, in case of phosphorescent emitters, low PLQYs (thus, disagreement between the theoretical and experimental maximum EQEs) can be obtained if quantum yields of singlet−triplet conversion (STC) efficiency of phosphorescent complexes are below 100 %, which is a typical case [51]. Apparently, because of that, experimental EQE of 22.6 % was reached for $(piq)_2Ir(acac)$-based devices despite experiment PLQY of 20% recorded for the emitter $(piq)_2Ir(acac)$ [50, 52]. Therefore, one of the highest experimental EQE values reported for $(piq)_2Ir(acac)$ based devices which reached 22.6 % was selected for the comparison with EQE values of our devices [52]. For example, device E demonstrated EQE of 15.9 % which is not far below of that observed for

the previously published $(piq)_2Ir(acac)$ based devices. To provide comparison of characteristics of **AcDbp** and **CzDbp** based devices with the reference devices, the concentration of $(piq)_2Ir(acac)$ dopant of 5 wt. % in light-emitting layer was selected. It is predictively possible to improve the efficiency of **AcDbp** and **CzDbp** based devices when the concentration of the $(piq)_2Ir(acac)$ dopant or/and thicknesses of additional layers are optimised.

Both charge-balance factors and efficiency of exciton production can be responsible for high EQE of device **E**. The TOF experiment showed, that the balance of hole and electron transport in the host **AcDbp** should be even better than that in **CzDbp.** However, device **D** did not show higher maximum EQE value than device **E** (**Fig. 8b**). The balance hole and electron transport of devices **F-H** should be also good. Taking into account the similarities/differences of hole-electron balance, the high efficiency of device **E** is partly attributed to harvesting of triplet excitons not only within phosphorescent emitter $(piq)_2Ir(acac)$ but also within the host **CzDbp** due to its TTA/TADF properties. Thus, the higher efficiency of device **E** is partly attributed to the higher efficiency of exciton production in comparison to that of the similar/reference devices **D, F-H**.

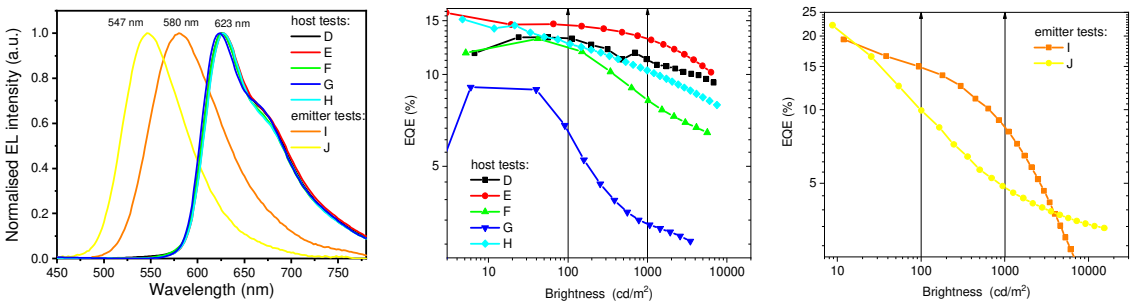

(a) **(b)** **(c)**

Fig. 8. EL spectra **(a)** and EQE efficiencies versus brightness **(b, c)** characteristics for the devices **D**-**J** with **AcDbp** and **CzDbp** as host or emitter

Not only compound **AcDbp** but also compound **CzDbp** are characterized by TADF. Thus, both the compounds are characterized by media dependent combination of TADF and TTA. TADF of compounds **AcDbp** and **CzDbp** is evident from very high maximum EQEs of 19.4 and 22.1 % observed for devices **I** and **J** based on the light-emitting layers **AcDbp**(20 wt. %):mCBP and **CzDbp**(20 wt. %):mCBP in which **AcDbp** or **CzDbp** were used as emitters in the same device structures as those of devices **D-H** (**Fig. 8c, Table 4**). Experimental maximum EQEs of 19.4 and 22.1 % observed for devices **I** and **J** respectively are not in agreement with the theoretical maximum EQEs (2.4 and 6.3%, assuming η_{out} of 0.3) estimated by formula (1) using PLQYs of 8 and 21 % of the light-emitting layers **AcDbp**(20 wt. %):mCBP and **CzDbp**(20 wt. %):mCBP, respectively (Table 3). This disagreement can be related to the possible loss mechanisms when the TADF molecules are optically excited as it was discussed in [53]. Devices **I** and **J** showed orange and yellow electroluminescence with CIE1931 colour coordinates of (0.513, 0.479) and (0.395, 0.578), respectively (**Fig. S26, S27, Table 4**). EL spectra were completely related to emissions of **AcDbp** or **CzDbp** indicating that hole-electron recombination took place within the light-emitting layers.

3.8. Mechanistic considerations

The triplet harvesting in **AcDbp** and **CzDbp** systems occurs by means of different either TADF or TTA mechanisms.

Static diagrams. In order to understand these differences, we focus first on the TADF mechanism. Following Adachi[54] and Gibson[55], energy diagrams representing only a selected set of excited states of **AcDbp** and **CzDbp** are shown in **Fig. 9a,b**. The energy of ^{3}LE for **AcDbp** (2.35 eV) was taken from the PH spectrum of the solution in THF at 77 K. Below, we consider that this energy value remains roughly similar in the case of the films of pure and doped in mCP **AcDbp**. Note that ^{3}LE energy level of **AcDbp** (in THF at 77 K) is

below ^{1}CT and ^{3}CT energy levels of **AcDbp** doped in mCP (2.56 eV and 2.53 eV, respectively), but is between ^{1}CT and ^{3}CT of non-doped **AcDbp** (2.39 eV and 2.26 eV, respectively). Based on these diagrams (**Fig. 9a**), interpretation of the delayed fluorescence in **AcDbp** seems to be straightforward: while mixing of ^{3}CT with ^{3}LE by means of IC makes the symmetry allowed ^{3}LE→^{1}CT rISC more efficient, the ΔE_{ST}(^{3}LE-^{1}CT) values seem to be very different depending on the conditions, adopting a relatively large upper-limit value of 0.21 eV for **AcDbp** doped in mCP, but much smaller (0.04 eV) for the pure compound (**Fig. 9a**). Consequently, TADF should be of different efficiencies for the layers of molecular dispersion of **AcDbp** in mCP and for the layer of pure compound, which seems to be incoherent with the close values of PLQY of 3 and 4 % respectively. A possible and partial explanation could stem from the practically orthogonal geometry of this compound: the prompt fluorescence is very inefficient, differences in TADF efficiency should be of secondary importance with respect of the total emission (prompt FL + TADF).

In the case of **CzDbp** , ^{1}CT and ^{3}CT energy levels (2.52 eV and 2.28 eV, respectively) were taken from the PL and PH spectra of the solutions in THF at 77 K. The experimental value of ^{3}LE for **CzDbp** is not accessible experimentally, given that T_1 is of CT nature. One could consider, however, the value of 2.35 eV measured for the ^{3}LE of **AcDbp** as a first approximation for the ^{3}LE state of **CzDbp** in THF at 77 K, which seems coherent with the similar space localization of this state for both the compounds only on the **Dbp** core (**Fig. S10**). In this case, ΔE_{ST} (^{3}LE-^{1}CT)=0.17 eV deduced from **Fig. 9b** for **CzDbp** is smaller than 0.21 eV estimated for **AcDbp** in mCP, for which the TADF seems efficient, thus making difficult to explain the absence of delayed fluorescence in the emission of **CzDbp**.

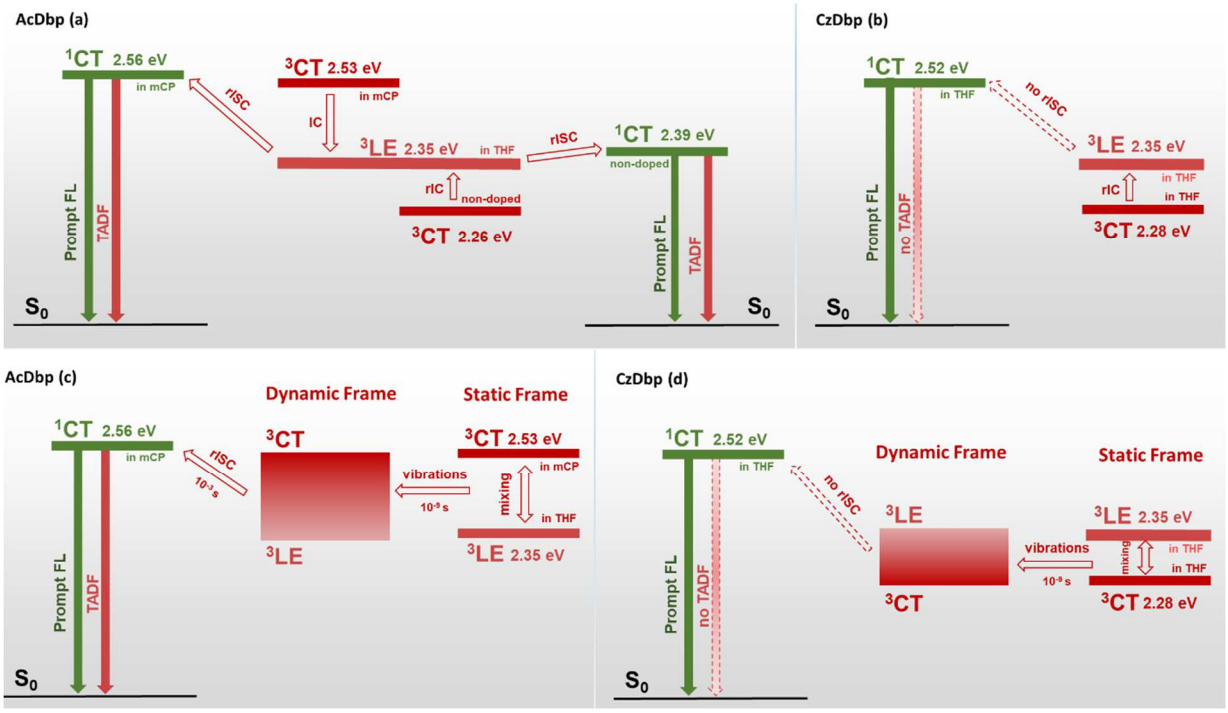

Fig. 9. Diagrams of excited states energies of **AcDbp (a)** and **CzDbp (b)**; diagrams illustrating the "dynamic" mechanism of mixing between LE and CT states through dihedral vibrations [56,57,58] in **AcDbp (c)** and **CzDbp (d)**

***Dynamic diagrams*.** The diagrams and comparisons presented above lack of the impact of mixing in the energy levels. In order to better understand this effect, we remember some of the milestone ideas and insights: (i) El Sayed's rule indicates that rISC between electronic states of the similar nature such as π-π* CT states is forbidden, thus preventing the interconversion between pure ^{3}CT and singlet ^{1}CT excited states in TADF compounds. (ii) The direct ^{3}LE-^{1}CT spin-orbit coupling was shown to be very small (merely several cm^{-1}) [56], failing consequently to explain the experimental rISC rate constants. (iii) The important information on the TADF mechanism was obtained by finding that the vibronic coupling between S_1 (T_1) and S_2 (T_2) is mandatory to promote $T_1 \rightarrow S_1$ rISC.[55,56] (iv) Calculations taking into account the contribution of IC or rIC between several low-lying excited states provide the crucial insight that ISC or rISC processes cannot be explained in a static frame;

dynamical processes through the dihedral-angle oscillations, which are by several orders of magnitude faster than ISC or rISC, were shown to be a key factor determining the TADF efficiency.[56,57,58] Indeed, the dihedral-angle oscillations and deformations around the D-A bond at excited states allow exploration of ensemble of conformations reachable at room temperature.

In addition to these findings, we suggest that the impact of these oscillations and deformations is the mixing between states: the nature of T_1 can change from pure CT to a mixed LE-CT state or vice-versa. This creates "new" excited states at intermediate energies between "static" ^{3}CT and ^{3}LE states, which are absent in the static-frame energy diagrams (deduced from the onset excitation energies). **Fig. 10a,b** show the dependence of the nature of "new" triplet state (T_*) from dihedral angle D-A size. These "dynamical" states allow molecules to profit from the LE contribution in T_1 to make the $T_1 \rightarrow S_1$ transition "allowed" (satisfy to El Sayed's rule) (**Fig. 10a**), hence increase the intensity of the $T_1 \rightarrow S_1$ transition (spin-orbit coupling, SOC), but also increase the intensity of $S_1 \rightarrow S_0$ transition, hence the PLQY of fluorescence. On the other hand, these oscillations and deformations could result in the increased ΔE_{ST} (**Fig. 10b**), which is detrimental for rISC. Nevertheless, at some point (a given geometry), the combination of SOC and ΔE_{ST} becomes convenient for effective rISC.[59] It is worth remembering the results from [59] showing the drastic decrease of rISC rates when ΔE_{ST} approaches 0.2 eV and beyond.

The ensemble of the above results and ideas,[56,57,58,59] are illustrated by means of a new diagram for **AcDbp** doped in mCP shown in **Fig. 9c**. In this figure, from right to left, the static frame with well-defined energies of ^{3}LE and ^{3}CT states (similarly to **Fig. 9a**) is followed by a "dynamic" frame, corresponding to dynamically created mixed ^{3}(LE-CT) states of intermediate energies between ^{3}LE-^{3}CT. Note, that dynamical energy levels below- or

above the static LE (CT) and CT (LE) could also be expected; nevertheless, we show in the dynamical diagrams only the energy levels in between those of LE- and CT.

In this context, while different rISC pathways would be predicted in a static frame, depending on the relative energy order between ^{3}LE and ^{3}CT, in the dynamic frame a fundamentally identical pathway could be predicted: $^3(CT\leftrightarrow LE) \xrightarrow{rISC} {}^1CT$. Considering now **AcDbp** doped in mCP, mixing of CT and LE characters in the same state is also accompanied by increase in the energy level somewhere in the mid-gap between ^{3}LE and ^{3}CT, resulting in reduced ΔE_{ST} as compared to the value of 0.21 eV deduced from the diagram shown in **Fig. 9a** thus making the TADF more efficient.

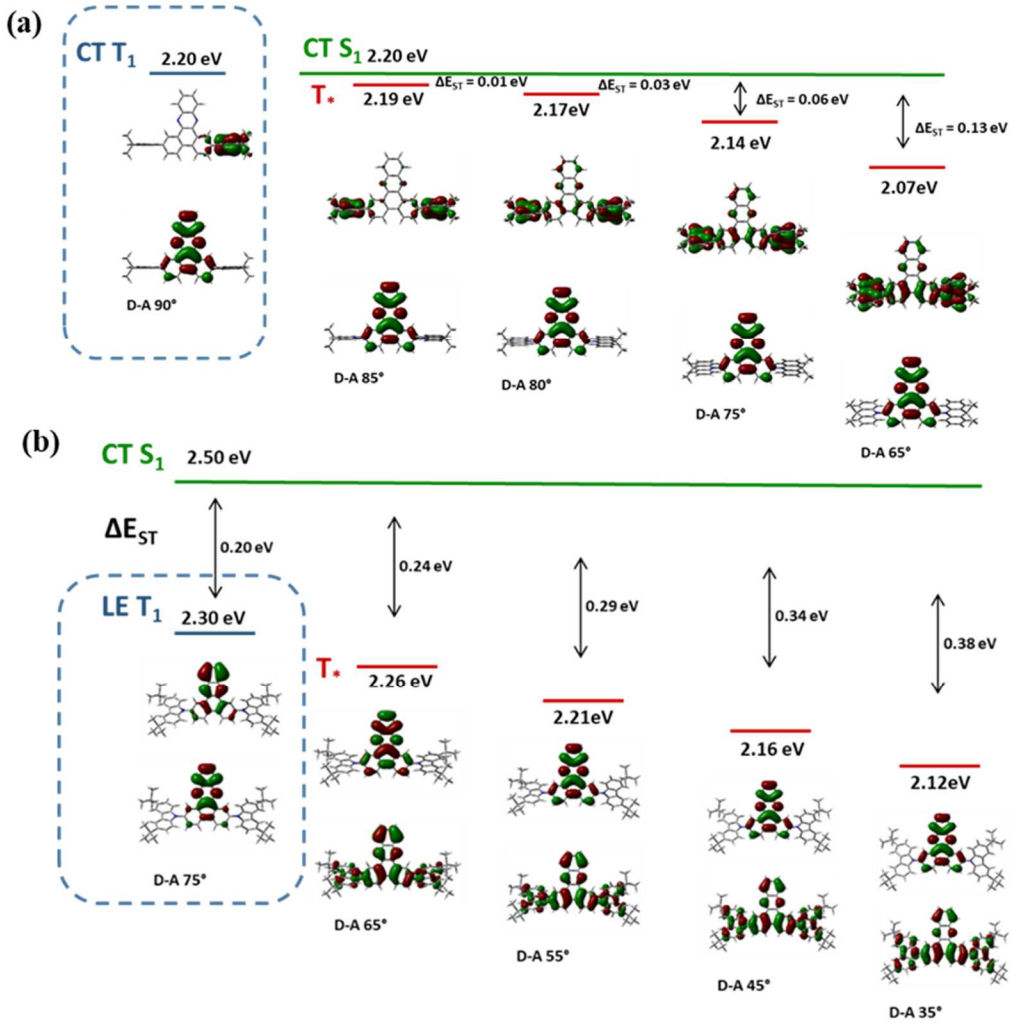

Fig. 10. Dependence of the nature of the first triplet state marked as T_* of **AcDbp (a)** and **CzDbp (b)** on the D-A dihedral angle (obtained from TD-DFT calculations at ω^{THF} B97XD).

In the case of **CzDbp** the same mechanism should hold true (**Fig. 9d**), but the energy of the mid-gap mixed states created "dynamically" (in-between ^{3}LE-^{3}CT) would correspond to increased ΔE_{ST} as compared to the value of 0.17 eV deduced from the diagram shown in **Fig. 9b**. This effect seems opposite to what occurs in case of **AcDbp**, and the increase of ΔE_{ST} from 0.17 eV to 0.24 eV could explain the inefficiency (absence) of delayed fluorescence.[59] Additionally, the theoretical (vertical) T^1 state for **CzDbp** is not a pure CT state, as shown in the experimental diagram of **Fig. 9b,d**, but a mixed ^{3}(LE-CT) one (**Fig. S28**). This means that the contribution of this state to the rISC by means of the second-order nonadiabatic coupling between ^{3}LE and ^{3}(CT-LE) would be less efficient than that between ^{3}LE and ^{3}(CT), again providing a possible explanation on the absence of delayed FL through the TADF channel in the case of **CzDbp**. The support to theoretical result related to the mixed ^{3}(LE-CT) nature of T_1 could rise from the shape of PL profiles of the films of pure **CzDbp** at very low temperatures (77-120-160 K, **Fig. 6c**. A weak vibrational character is visible in PL spectra, that we assume originating from phosphorescence contribution related to a mixed ^{3}(LE-CT) emitting state.

The above discussion provides possible explanations of the absence of triplet harvesting by means of TADF mechanism for **CzDbp** in THF and TOL solutions as well as in non-doped and doped in mCP layers. While, device **J** with **CzDbp** as emitter in mCBP demonstrating EQE of 22.1 % shows that triplet harvesting via TADF can occur, thus there are media in which **CzDbp** exhibit efficient TADF.

***Triplet-triplet annihilation*.** Our findings indicate that degassing of THF and TOL solutions of **CzDbp** results in increase of PLQY by 16% of both solutions. This means that the triplet

states do play a role in the PL of **CzDbp**, which should consequently be realized through a channel different from TADF being as fast as prompt fluorescence. One possible mechanism could be TTA, as shown in the section "Photophysical properties". Indeed, integrated PL intensities versus different excitation intensities give slope values higher than unity for **CzDbp** and **AcDbp** (**Fig. 4b**). Thus evidencing that the TTA mechanism contributes to the triplet harvesting in both compounds [48,49], when **CzDbp** as well as **AcDbp** plays the roles of both the synthesiser and the annihilator. This is in agreement with the higher slope than unity for brightness versus current density plots for devices **A** (1.191) and **B** (1.299) containing **AcDbp** and **CzDbp**, respectively. In addition, this is coherent with the fact that the maximum wavelengths of the PL spectra of **CzDbp** recorded in degassed and in-air conditions are identical (**Fig. 5c**) and is consistent with the assumption that S_n, the new singlet state created by the interaction of two triplet molecules, relax to S_1 before radiative transition towards the ground state. The increase of PLQY by16% after deoxygenation of the solution is in good agreement with the reported maximum theoretical value of 20%.[9,60] Concerning to the fast TTA supposed in the case of **CzDbp**, the experimental support comes from the fast TTA (in ns range; $k_{TTA} > 10^9$ $M^{-1} \cdot s^{-1}$) previously reported, for example, for perylene [61] and many other TTA materials [10].

4. Conclusions

We have synthesized two new D-A-D type molecules, **CzDbp** and **AcDbp**, and have characterized them by means of experimental and theoretical methods. The solid layers of both the semiconductors exhibit bipolar charge transport with drift mobilities exceeding 10^{-3} cm^2/Vs at high electric fields. The compounds are able to harvest triplet excitons by either triplet-triplet annihilation (TTA) or thermally activated delayed fluorescence (TADF) mechanisms.

The experimental optical absorption spectra of **AcDbp** and **CzDbp** in different media indicate presence of very-low intensity CT-tails for both the compounds, the intensity of which increases with the increasing concentration of compounds. Photoluminescence spectra and decay curves of **AcDbp** revealed the presence of delayed fluorescence occurring through the TADF mechanism. In the case of **CzDbp**, no delayed fluorescence was observed, however, triplet exciton harvesting through the TTA mechanism was evidenced. The absence of delayed fluorescence is assumed to stem from a combination of two effects. Compared to TADF timescales observed for **AcDbp** (10^{-3} s), faster triplet harvesting in **CzDbp** through TTA channel was evidenced through electroluminescence. The timescale is supposed to be similar to emission timescales of the prompt fluorescence. This leads to an increase of PLQY of the solutions by 16% after degassing. Independently from the faster (hence competitive) TTA channel for triplet harvesting, the TADF mechanism was found to be inefficient in the case of **CzDbp**, due to a combination of large singlet-triplet splitting reaching 0.24 eV, and limited contribution from the mixing (second-order nonadiabatic coupling) between ^{3}LE and ^{3}(CT-LE). This is due to the relatively small dihedral angles in **CzDbp** resulting in mixing of LE and CT characters in T_1, thus reducing the contribution of CT character to the T_1-S_1 rISC.

From a fundamental standpoint, our results demonstrate that triplet harvesting in donor acceptor molecules with small singlet-triplet splitting is not necessary related to TADF as it is widely accepted, but can proceed through eventually faster and competitive TTA mechanism. "Dynamic" state-energy diagrams, which consider the dynamical CT-LE mixing through fast vibrational motions allow better understanding of the experimental results related to TADF mechanism, as compared to the static state-energy diagrams.

In view of the interesting properties of **AcDbp** and **CzDbp**, these compounds were used as hosts in red PHOLEDs. The device with **CzDbp** host exhibited superior parameters of electrophosphorescence allowing to achieve higher external quantum efficiency of 15.9 % as

well as lower efficiency roll-off in comparison to those of the device based on the widely utilised mCP, mCBP, NPB and nBPhen hosts. External quantum efficiencies of 19.4% and 22.1% for doped yellow and orange devices were achieved when the compounds **CzDbp** and **AcDbp** were used as TADF/TTA emitters, respectively.

Acknowledgements

This project has received funding from European Social Fund (project No 09.3.3-LMT-K-712-02-0106) under grant agreement with the Research Council of Lithuania (LMTLT)

References

[1] Y. Liu, C. Li, Z. Ren, S. Yan, M. R. Bryce, All-organic thermally activated delayed fluorescence materials for organic light-emitting diodes, Nat. Rev. Mater. 18020 (2018) 1-20. https://doi:10.1038/natrevmats.2018.20

[2] L. Zhang, K.W. Cheah, Thermally activated delayed fluorescence host for high performance organic light-emitting diodes, Sci. Rep. 8832 (2018) 1-6. https://doi:10.1038/s41598-018-27238-y

[3] X. Ban, F. Chen, Y. Liu, J. Pan, A. Zhu, W. Jiang, Y. Sun, Design of efficient thermally activated delayed fluorescence blue host for high performance solution-processed hybrid white organic light emitting diodes, Chem. Sci. 10 (2019) 3054-3064. https://doi.org/10.1039/C8SC05456H

[4] Z. Yang, Z. Mao, Z. Xie, Y. Zhang, S. Liu, J. Zhao, J. Xu, Z. Chi, M. P. Aldred, Recent advances in organic thermally activated delayed fluorescence materials, Chem. Soc. Rev. 46 (2017) 915-1016. https://doi.org/10.1039/C6CS00368K

[5] M.K. Etherington, J. Gibson, H.F. Higginbotham, T.J. Penfold, A.P. Monkman, Revealing the spin-vibronic coupling mechanism of thermally activated delayed fluorescence, Nat. Commun. 7 (2016) 13680 1-7. https://doi:10.1038/ncomms13680

[6]G. Méhes, K. Goushia, W.J. Potscavage Jr. C. Adachi, Influence of host matrix on thermally-activated delayed fluorescence: Effects on emission lifetime, photoluminescence quantum yield, and device performance, Org. Electron. 15 (2014) 2027-2037, https://doi.org/10.1016/j.orgel.2014.05.027

[7] S.K. Lower, M.A. El-Sayed, The triplet state and molecular electronic processes in organic molecules, Chem. Rev. 66 (1966) 199-241, https://doi.org/10.1021/cr60240a004

[8] D. M. Mayder, C. M. Tonge, Z. M. Hudson, Thermally activated delayedfFluorescence in 1,3,4-oxadiazoles with π-extended donors, J. Org. Chem. 85 (2020) 11094–11103. https://doi.org/10.1021/acs.joc.0c00908

[9] X. Qiao, D. Ma. Nonlinear optoelectronic processes in organic optoelectronic devices: Triplet-triplet annihilation and singlet fission, Mater. Sci. Eng. R 139 (2020) 100519 1-38. https://doi.org/10.1016/j.mser.2019.100519

[10] J. Zhou, Q. Liu, W. Feng, Y. Sun, F. Li. Upconversion Luminescent Materials: Advances and Applications, Chem. Rev. 115 (2015) 395–465. https://doi.org/10.1021/cr400478f

[11] J. Liu, Z. Li, T. Hu, X. Wei, R. Wang, X. Hu, Y. Liu, Y. Yi, Y. Yamada-Takamura, Y. Wang, P. Wang, Experimental evidence for “Hot Exciton” thermally activated delayed fluorescence emitters, Adv. Optical Mater. 7 (2019) 1801190 1-9. https://doi.org/10.1002/adom.201801190

[12] Y. Xu, X. Liang, X. Zhou, P. Yuan, J. Zhou, C. Wang, B. Li, D. Hu, X. Qiao, X. Jiang, L. Liu, S-J. Su, D. Ma, Y. Ma, Highly efficient blue fluorescent OLEDs based on

upper level triplet–singlet intersystem crossing, Adv. Mater. 31 (2019) 1807388 1-8. https://doi.org/10.1002/adma.201807388

[13] J.-H. Lee, C.-H. Chen, P.-H. Lee, H.-Y. Lin, M-K Leung, T.-L. Chiu, C.-F. Lin, Blue organic light-emitting diodes: current status, challenges, and future outlook, J. Mater. Chem. C, 2019,7, 5874-5888. https://doi.org/10.1039/C9TC00204A

[14] N.A. Kukhta, T. Matulaitis, D. Volyniuk, K. Ivaniuk, P. Turyk, P. Stakhira, J.V. Grazulevicius, A. P. Monkman, Deep-blue high-efficiency TTA OLED using para- and meta-conjugated cyanotriphenylbenzene and carbazole derivatives as emitter and host, J. Phys. Chem. Lett. 8 (2017) 6199–6205. https://doi.org/10.1021/acs.jpclett.7b02867

[15] B. Wex, B.R. Kaafarani, Perspective on carbazole-based organic compounds as emitters and hosts in TADF applications, J. Mater. Chem. C, **5** (2017) 8622-8653. https://doi.org/10.1039/C7TC02156A

[16] O. Bezvikonnyi, D. Gudeika, D. Volyniuk, M. Rutkis, J.V. Grazulevicius, Diphenylsulfone-based hosts for electroluminescent devices: Effect of donor substituents, Dyes Pigm. 175 (2020) 108104 1-10. https://doi.org/10.1016/j.dyepig.2019.108104

[17] M.-H. Hsin, C.-Y. Lee, Y.-C. Chen, P.-Y. Chen, Y.-H. Chen, H.-H. Lu, Y.-H. Lin, B.-Y. Lin, M.-Z. Lee, T.-L. Chiu, C.-F. Lin, J.-H. Lee, 89.3% Lifetime elongation of blue TTA-OLED with assistant host, SID 2016 DIGEST, 1727-1729. https://doi.org/10.1002/sdtp.11043

[18] X. Song, D. Zhang, Y. Lu, C. Yin, L. Understanding and Manipulating the Interplay of Wide-Energy-Gap Host and TADF Sensitizer in High-Performance Fluorescence OLEDs, Adv. Mater. 2019, 31, 1901923:1-9. https://10.1002/adma.201901923

[19] X. Chen, C. Xu, T. Wang, C. Zhou, J. Du, Z. Wang, H. Xu, T. Xie, G. Bi, J. Jiang, X. Zhang, J.N. Demas, C.O. Trindle, Y. Luo and G. Zhang, Versatile Room-Temperature-Phosphorescent Materials Prepared from N-Substituted Naphthalimides: Emission

Enhancement and Chemical Conjugation, Angew. Chem. Int. Ed. 55 (2016) 9872 –9876. https://doi.org/10.1002/anie.201601252

[20] T. Higuchi, H. Nakanotani and C. Adachi, High-efficiency white organic light-emitting diodes based on a blue thermally activated delayed fluorescent emitter combined with green and red fluorescent emitters, Adv. Mater. 27 (2015) 2019–2023. https://doi.org/10.1002/adma.201404967

[21] F. Khana, E. Urbonas, D. Volyniuk, J.V. Grazulevicius, S.M. Mobin,, R. Misra, White hyperelectrofluorescence from solution-processable OLEDs based on phenothiazine substituted tetraphenylethylene derivatives. J. Mater. Chem. C, 2020, Accepted Manuscript. https://doi.org/10.1039/D0TC03136D

[22] H. Sun, C. Zhong, J.-L. Brédas. Reliable prediction with tuned range-separated functionals of the singlet–triplet gap in organic emitters for thermally activated delayed fluorescence, J. Chem. Theory Comput. 11 (2015) 3851–3858. https://doi.org/10.1021/acs.jctc.5b00431

[23] S. Boxi, D. Jana, Partha, P. Parui, B.K. Ghorai, Dibenzo[a, c]phenazine-based donor-acceptor (D–A) tetra branched molecules: fine tuning of optical properties, 3 (2018) 6953-6959. https://doi.org/10.1002/slct.201801500

[24] C. Zhou, S. Xiao, Man Wang, W. Jiang, H. Liu, S. Zhang, B. Yang, Modulation of excited state property based on benzo[a, c]phenazine acceptor: three typical excited states and electroluminescence performance, Front. Chem. 7 (2019) 141 1-10. https://doi.org/10.3389/fchem.2019.00141

[25] F.-M. Xie, Z.-D. An, M. Xie, Y.-Q. Li, G.-H. Zhang, S.-J. Zou, L. Chen, J.-D. Chen, T. Cheng, J.-X. Tang, tert-Butyl substituted hetero-donor TADF compounds for efficient solution-processed non-doped blue OLEDs, J. Mater. Chem. C, 8 (2020) 5769-5776. https://doi.org/10.1039/D0TC00718H

[26] Y. Im, M. Kim, Y.J. Cho, J.-A Seo, K.S Yook, J.Y. Lee, Molecular design strategy of organic thermally activated delayed fluorescence emitters, Chem. Mater. 29 (2017) 1946−1963. https://doi.org/0.1021/acs.chemmater.6b05324

[27] A. Ivanauskaite, R. Lygaitis, S. Raisys, K. Kazlauskas, G. Kreiza, D. Volyniuk, D. Gudeika, S. Jursenas, J.V. Grazulevicius, Structure–property relationship of blue solid state emissive phenanthroimidazole derivatives, Phys. Chem. Chem. Phys. 19 (2017) 16737-16748. https://doi.org/10.1039/C7CP02248D

[28] K. Yamaguchi, Y. Esaki, T. Matsushima, C. Adachi, A 1,4,5,8,9,11-hexaazatriphenylenehexacarbonitrile (HAT-CN) transport layer with high electron mobility for thick organic light-emitting diodes, AIP Adv. 10 (2020) 055304:1-5. https://doi.org/10.1063/5.0007310

[29] F. M. Xie, H. Z. Li, G. L. Dai, Y. Q. Li, T. Cheng, M. Xie, J. X. Tang, X. Zhao, Rational molecular design of dibenzo[a,c]phenazine-based thermally activated delayed fluorescence emitters for orange-red OLEDs with EQE up to 22.0%, ACS Appl. Mater. Interfaces 2020, 12, 16, 18730–18738.

[30] W. Liu, X. Luo, Y. Bao, Y. P. Liu, G.-H. Ning, I. Abdelwahab, L. Li, C. T. Nai, Z. G. Hu, D. Zhao, B. Liu, S. Y. Quek, K. P. Loh, A two-dimensional conjugated aromatic polymer via C–C coupling reaction, Nat. Chem. 9 (2017) 563–570. https://doi.org/10.1038/nchem.2696

[31] E. K. Unver, S. Tarkuc, Y. A. Udum, C. Tanyeli, L. Toppare, Effect of conjugated core building block dibenzo[a,c]phenazine unit on π-conjugated electrochromic polymers: Red-shifted absorption, J. Polym. Sci. A Polym. Chem. 48 (2010) 1714–1720. https://doi.org/10.1002/pola.23935

[32] P. Moonsin, N. Prachumrak, R. Rattanawan, T. Keawin, S. Jungsuttiwong, T. Sudyoadsuk, V. Promarak, Carbazole dendronised triphenylamines as solution processed

high Tg amorphous hole-transporting materials for organic electroluminescent devices, Chem. Commun. 48 (2012) 3382-3384. https://doi.org/10.1039/C2CC16878B

[33] W. Kohn, L.J. Sham, Self-consistent equations including exchange and correlation effects, Phys. Rev. 140 (1965) A1133-A1138. https://doi.org/10.1103/PhysRev.140.A1133

[34] E.K.U Gross, W. Kohn, Time-dependent density-functional theory. Adv. Quantum Chem. 21 (1990) 255-291. https://doi.org/10.1016/S0065-3276(08)60600-0

[35] R. Baurnschmitt, R. Ahlrichs, Treatment of electronic excitations within the adiabatic approximation of time dependent density functional theory, Chem. Phys. Lett. 256 (1996) 454-464. https://doi.org/10.1016/0009-2614(96)00440-X

[36] M.E. Casida, C. Jamorski, K.C. Casida, D.R. Salahub, Molecular excitation energies to high-lying bound states from time-dependent density-functional response theory: characterization and correction of the time-dependent local density approximation ionization thresholdJ. Chem. Phys. 108 (1998) 4439-4449. https://doi.org/10.1063/1.475855

[37] E. Miyamoto, Y. Yamaguchi, M. Yokoyama, Ionization potential of organic pigment film by atmospheric photoelectron emission analysis, Electrophotography 28 (1989) 364-370. https://doi.org/10.11370/isjepj.28.364

[38] S. Okamoto, K. Tanaka, Y. Izumi, H. Adachi, T. Yamaji, T. Suzuki, Simple measurements of quantum efficiency in organic electroluminescent devices, Jpn. J. Appl. Phys. 40 (2001) 783-84. https://doi.org/ 10.1143/JJAP.40.L783

[39] Z. Zheng, D.A. Egger, J.-L. Brédas, L. Kronik, V. Coropceanu, Effect of solid-state polarization on charge-transfer excitations and transport levels at organic interfaces from a screened range-separated hybrid functional, J. Phys. Chem. Lett. 8 (2017) 3277–3283. https://doi.org/10.1021/acs.jpclett.7b01276

[40] V. Mimaite, J. V. Grazulevicius, R. Laurinaviciute, D. Volyniuk, V. Jankauskas, G. Sini, Can hydrogen bonds improve the hole-mobility in amorphous organic semiconductors?

Experimental and theoretical insights, J. Mater. Chem. C 3 (2015) 11660-11674. https://doi.org/10.1039/C5TC02534F

[41] J. Grüne, N. Bunzmann, M. Meinecke, V. Dyakonov, A. Sperlich. Kinetic modeling of transient electroluminescence reveals TTA as an efficiency-limiting process in exciplex-based TADF OLEDs. J. Phys. Chem. C. (2020). https://doi.org/10.1021/acs.jpcc.0c06528.

[42] A.A. Rudnick, S. Bagnich, D. Wagner, S. Athanasopoulos, P. Strohriegl, A. Köhler, The influence of torsion on excimer formation in bipolar host materials for blue phosphorescent OLEDs, J. Chem. Phys. 144 (2016) 214906:1-6. https://doi.org/10.1063/1.4953102

[43] Y. Wang, Y. Yi, P. Wang, Y. Chen, X. Wei, R. Wang, Z. Li, Y. Liu, R. Duan, J. Liu and Y. Yamada-Takamura, Triplet decay-induced negative temperature dependence of the transient Photoluminescence decay of thermally activated delayed fluorescence emitter. J. Mater. Chem. C, 2017, DOI: 10.1039/C7TC04025C.

[44] A.E. Nikolaenko, M. Cass, F. Bourcet, D. Mohamad, M. Roberts, Thermally activated delayed fluorescence in polymers: A new route toward highly efficient solution processable OLEDs, Adv. Mater. 27 (2015) 7236-7240. https://doi.org/10.1002/adma.201501090

[45] J.U. Kim, I.S. Park, C.-Y. Chan, M. Tanaka, Y. Tsuchiya, H. Nakanotani, C. Adachi, Nanosecond-time-scale delayed fluorescence molecule for deep-blue OLEDs with small efficiency rolloff, Nat. Commun. 11 (2020) 1765 1-8. https://doi.org/10.1038/s41467-020-15558-5

[46] N. Bunzmann, S. Weissenseel, L. Kudriashova, J. Gruene, B. Krugmann, J. V. Grazulevicius, A. Sperlich, V. Dyakonov, Optically and electrically excited intermediate

electronic states in donor:acceptor based OLEDs, Mater. Horiz. 7 (2020) 1126-1137. https://doi.org/10.1039/C9MH01475F

[47] C.-G. Zhen, Y.-F. Dai, W.-J. Zeng, Z. Ma, Z.-K. Chen, J. Kieffer, Achieving highly efficient fluorescent blue organic light-emitting diodes through optimizing molecular structures and device configuration, Adv. Funct. Mater. 21 (2011) 699–707. https://doi.org/10.1002/adfm.201002165

[48] P.-Y. Chou, H.-H. Chou, Y.-H. Chen, T.-H. Su, C.-Y. Liao, H.-W. Lin, W.-C. Lin, H.-Y. Yen, I.-C. Chena, C.-H. Cheng, Efficient delayed fluorescence via triplet–triplet annihilation for deep-blue electroluminescence, Chem. Commun. 50 (2014) 6869-6871. https://doi.org/10.1039/C4CC01851F

[49] C. Ganzorig, M. Fujihira, A possible mechanism for enhanced electrofluorescence emission through triplet–triplet annihilation in organic electroluminescent devices, Appl. Phys. Lett. 81 (2002) 3137-3139. https://doi.org/10.1063/1.1515129

[50] Y.-J. Su, H.-L. Huang, C.-L. Li, C.-H. Chien, Y.-T. Tao, P.-T. Chou, S. Datta, R.-S. Liu. Highly efficient red electrophosphorescent devices based on iridium isoquinoline complexes: remarkable external quantum efficiency over a wide range of current. Adv. Mater. 15(11) (2003) 884–888. https://doi.org/10.1002/adma.200304630.

[51] S. Tofighi, P. Zhao, R.M. O'Donnell, J. Shi, P.Y. Zavalij, M.V. Bondar, D.J. Hagan, E.W. Van Stryland. Fast triplet population in iridium(III) complexes with less than unity singlet to triplet quantum yield. J. Phys. Chem. C, 123 (2019) 13846−13855. https://doi.org/10.1021/acs.jpcc.9b00539.

[52] C.-H. Fan, P. Sun, T.-H. Su, C.-H. Cheng. Host and dopant materials for idealized deep-red organic electrophosphorescence devices. Adv. Mater. 23 (2011)2981–2985. https://doi.org/10.1002/adma.201100610.

[53] F.B. Dias, J. Santos, D.R. Graves, P. Data, R.S. Nobuyasu, M.A. Fox, A.S. Batsanov, T. Palmeira, M.N. Berberan-Santos, M.R. Bryce, A.P. Monkman. The role of local triplet excited states and d-a relative orientation in thermally activated delayed fluorescence: photophysics and devices. Adv. Sci. 3 (2016) 1600080 1–10. https://doi.org/10.1002/advs.201600080.

[54] T. Kobayashi, A. Niwa, K. Takaki, S. Haseyama, T. Nagase, K. Goushi, C. Adachi, H. Naito, Contributions of a higher triplet excited state to the emission properties of a thermally activated delayed-fluorescence emitter, Phys. Rev. Applied. 7 (2017) 034002 1-10. https://doi.org/10.1103/PhysRevApplied.7.034002

[55] J. Gibson, A.P. Monkman, T.J. Penfold, The importance of vibronic coupling for efficient reverse intersystem crossing in thermally activated delayed fluorescence molecules, Commun. 17 (2016) 2956-2961. https://doi.org/10.1002/cphc.201600662

[56] X.-K. Chen, S.-F. Zhang, J.-X. Fan, A.-M. Ren, Nature of highly efficient thermally activated delayed fluorescence in organic light-emitting diode emitters: nonadiabatic effect between excited States, J. Phys. Chem. C. 119 (2015) 9728–9733. https://doi.org/10.1021/acs.jpcc.5b00276

[57] B. R. Henry, W. Siebrand, Spin–orbit coupling in aromatic hydrocarbons. Analysis of nonradiative transitions between singlet and triplet states in benzene and naphthalene, J. Chem. Phys. 54 (1971) 1072-1085. https://doi.org/10.1063/1.1674940

[58] Y. Olivier, B. Yurash, L. Muccioli, G. D'Avino, O. Mikhnenko, J. C. Sancho-García, C. Adachi, T.-Q. Nguyen, D. Beljonne, Nature of the singlet and triplet excitations mediating thermally activated delayed fluorescence, Phys. Rev. Materials. 1 (2017) 075602 1-6. https://doi.org/10.1103/PhysRevMaterials.1.075602

[59] P.K. Samanta, D. Kim, V. Coropceanu, J.-L Brédas, Up-conversion intersystem crossing rates in organic emitters for thermally activated delayed fluorescence: Impact of the

nature of singlet vs triplet excited states, J. Am. Chem. Soc. 139 (2017) 4042−4051. https://doi.org/10.1021/jacs.6b12124

[60] R. Ieuji, K. Goushi, C. Adachi, Triplet–triplet upconversion enhanced by spin–orbit coupling in organic light-emitting diodes, Nat. Commun. 10 (2019) 5283 1-10. https://doi.org/10.1038/s41467-019-13044-1

[61] C. Ye, V. Gray, J. Martensson, K. Borjesson, Annihilation versus excimer formation by the triplet pair in triplet–triplet annihilation photon upconversion, J. Am. Chem. Soc. 141 (2019) 9578−9584. https://doi.org/10.1021/jacs.9b02302